STUDY OF THE APPLICATION OF PHOTOELASTICITY TO THE INVESTIGATION OF STRESS WAVES

Thesis by

George Walter Sutton

In Partial Fulfillment of the Requirements

for the Degree of

Doctor of Philosophy

California Institute of Technology

Pasadena, California

1955

ACKNOWLEDGMENTS

The author wishes to thank Dr. Milton S. Plesset for suggesting this investigation as part of the extensive cavitation research being conducted at the Hydrodynamics Laboratory; Dr. Albert T. Ellis for assisting the author in innumerable instances in the experimental work; Dr. Donald E. Hudson for his guidance in the measurement of transient strains; Dr. Max L. Williams for his advice and experience concerning photoelasticity; Dr. George W. Housner and Dr. Julian D. Cole for their many suggestions concerning the analysis of stress waves.

This study was supported in part by a National Science Foundation Fellowship, the AiResearch Fellowship, and the Office of Naval Research.

ABSTRACT

The object of this investigation is to determine the suitability of photoelasticity for the purpose of quantitatively investigating stress waves in solids. Specifically, procedures for determining the dynamic mechanical and optical properties of a common photoelastic plastic, CR-39, were investigated, as well as the techniques for recording dynamic fringe lines.

The dynamic mechanical properties of CR-39 were determined from the frequency and decay of free-free longitudinal vibrations of bars. It was found that CR-39 is a viscoelastic plastic whose wave speed, complex modulus, and damping depends on frequency. The stress-strain relationship for CR-39 was found to be slightly nonlinear.

The birefringent properties of CR-39 were determined from impact tests in which the fringe order was detected by a phototube, and strain was measured by means of bonded wire strain gages. The results show that CR-39 has a strain-fringe constant of 3.42×10^{-4} in/fringe $\pm$ 3%, which is the same as the static value within experimental error. Thus this constant is independent of the rate of loading. CR-39 is not stress-birefringent, which is the usual law quoted for photoelastic plastics.

An approximate theory of longitudinal stress waves in elastic bars is derived, which shows that the Boussinesq theory, if used to calculate the stress-fringe constant from sharp impacts, leads to serious error.

Using the Ellis camera, strain wave isochromatics can be photographed at framing rates up to 400,000 per second. An RCA 1P21 multiplier phototube was found to be extremely sensitive to optical retardation, by using it to detect the time duration of transient strains caused by cavitation. The tube has a frequency response of at least 18 megacycles.

TABLE OF CONTENTS

I INTRODUCTION

Dynamic photoelasticity, until now, has not proven to be a practical method of experimentally investigating stress waves. One limitation, which is more fully discussed on pages 30 and 31, was the inadequate techniques used to record fringe lines. Another limitation, described more completely on pages 22 to 29, was the complete lack of quantitatively accurate data regarding the mechanical and optical properties of photoelastic plastics during dynamic loading. The little data that was available had been obtained under specific loading conditions by comparing the fringe order of the wave to the value of stress that was calculated from the Boussinesq theory of stress waves in bars. This same theory was also used to calculate the elastic modulus from the experimental values of the longitudinal wave speed. Extrapolation of this data to other dynamic loading conditions is not warranted.

It is the object of this investigation to determine the suitability of photoelasticity for the purpose of quantitatively investigating stress waves in solids. This main objective is broken down into a number of specific objectives, which divide this thesis into its remaining sections. The specific objective of each section is outlined below, and discussions of previous investigations are made in the appropriate part.

Part II contains the first of these objectives, which is the development of methods of determining the optical and mechanical properties of photoelastic plastics, not only for dynamic loading conditions, but for static loading conditions as well. These methods are applied to a common photoelastic plastic, CR-39, the choice of

which was largely a matter of convenience. The optical tests are such that stress birefringence can be distinguished clearly from strain birefringence.

Part III contains the second objective, which is the adaption of an ultra-high speed motion picture camera to dynamic photoelasticity. A full frame camera has the obvious advantage of being capable of photographing the entire specimen, but the time resolution is limited by the specific camera used.

Part IV contains the third objective, which is the attainment of the best possible time resolution by the use of a multiplier phototube. The stress waves caused by cavitation is the specific phenomenon investigated with the photocell, because of the extremely short time durations and localization usually associated with cavitation.

Part V contains the final objective, which is a more accurate analysis of longitudinal stress waves in elastic bars. The results of this analysis are to be compared to the Boussinesq theory to determine whether the latter theory is sufficiently accurate to be utilized for the computation of the elastic modulus and stress-fringe constants for photoelastic plastics.

Part VI contains the conclusions of this study, based upon the results of the investigations of the previous parts.

II MECHANICAL AND OPTICAL PROPERTIES OF CR-39

In order to interpret quantitatively the results of photoelastic experiments, the mechanical and optical properties of the photoelastic plastic must be known. No reliable dynamic data was available in the literature; hence the selection of a plastic was based almost solely on availability and ease of machining. In addition it appeared desirable to use a relatively stiff and hard photoelastic plastic. Such a plastic is CR-39, which is available in clear sheets and is relatively easy to machine. It is a thermosetting polymer of allyl diglycol carbonate. According to Coolidge (1),

> "Essentially, its manufacture consists of reacting phosgene with diethylene glycol to obtain a chloroformate which is then esterified with allyl alcohol to produce the diglycol carbonate monomer. This monomer is polymerized by heating in the presence of a catalyst such as benzoyl peroxide to form the hard, strong, infusible, insoluble, clear, substantially colorless substance known as CR-39. The commercially obtainable sheets of CR-39 are cast-polymerized between glass plates, producing optically beautiful surfaces."

STATIC PROPERTIES OF CR-39

Although it is the dynamic properties of CR-39 that are of main interest, the determination of the static properties is also of interest, since the dynamic properties then can be compared to the static values. This is of importance, because all other

investigators in dynamic photoelasticity have found differences in the optical retardation for dynamic as against static loading conditions.

Static studies of the properties of CR-39 have been made by the manufacturer, the Cast Optics Corporation of Riverside, Connecticut; and by Coolidge (1). Their results are compared to those of this study in Table I below.

Table I

Static Properties of CR-39

Property	Manufacturer's Data	Coolidge's Data	Author's Data
Tensile strength, psi	5000-6000	7000*	----
Elastic Modulus, psi	$2.5\text{-}3.3 \times 10^5$	2.7×10^5	3.76×10^5 *
Poisson's Ratio	-----	----	0.443
Strain Creep	-----	yes	yes (see text)
Specific Gravity	1.31	----	1.326
Stress-Fringe Constant, psi-in/fringe, 5461 Å	86.6	78.5**	90.8*
Optical Creep	none	20%/180min	yes(see text)
Strain-Fringe Constant, in/fringe	-----	----	3.48×10^{-4}
Refractive index N_D	1.50398	----	-----

* Immediately after application of load

** Stress was increased by increments to 4300 psi during 14 minutes; time between increments varied from one to two minutes.

Coolidge determined the mechanical properties on a tensile specimen for which the load was increased by increments every 10 minutes. The optical properties were determined in a similar fashion but with smaller time increments. Optical creep was observed in a beam subjected to pure bending. As will be discussed later, all three of these procedures are subject to serious error.

EXPERIMENTAL PROCEDURE

Static tests were made on a simple tensile specimen with a working section 0.252 inches thick, width of 0.500 inches, and 3 inches long. Baldwin A-8 strain gages were cemented with Duco cement to the front and back of the specimen in both the longitudinal and transverse directions. Strain was indicated by a Baldwin-Foxboro portable strain indicator, which could be read to within 10 microinches per inch. The strain gage constant, as given by the manufacturer, is supposed to be accurate to $\pm 2\%$.

The specimen was placed in the spherical mirror polariscope designed by Goetz (2). The light source was a low pressure mercury vapor lamp, used with a Wratten 77A filter to produce monochromatic light of 5461 Å wave length. The fringe order in the specimen was determined by a Babinet-Soleil compensator that could be read to within 1/100 of a fringe line. Both the strain indicator and compensator were calibrated; in addition, the strain gages were checked against the readings of two Huggenberger extensometers.

Creep tests were made by applying constant loads to the tensile specimen for 180 minutes during which time the strain and fringe order were determined; the load was then removed and readings were made for another 180 minutes.

REDUCTION OF DATA

Figure 1 shows the results of a typical creep test. The fringe order N has been determined with the Babinet-Soleil compensator; strain was read directly from the Baldwin-Foxboro

strain indicator. The strain in the longitudinal direction is e_1; in the transverse direction e_2.

Two corrections must be made to the creep data, one to correct for changes in thickness of the specimen when strained; the other for erroneous strain gage readings. As for the first correction, the fringe order is supposed to be directly proportional to the thickness of the specimen, hence the value of the fringe order N must be multiplied by $(1 - e_2)$ in order that N be based on original thickness.

As for the second correction, the A-8 strain gage readings of Fig. 1 show that after 3 days, the birefringence of the specimen has virtually disappeared, but the strain gages still have a finite reading. In order to determine whether the gages were in error, a tensile stress of 1300 psi was applied in order to compare the A-8 gages with two Huggenberger mechanical extensometers. The Huggenbergers were used immediately after calibration, and could be read to within $\pm$ 10 microinches per inch. The results indicated that the A-8 wire strain gages were in error, and must be multiplied by the factors in Table II to obtain the Huggenberger readings.

When the load was removed at 180 minutes after application, the wire strain gages read approximately ten times that of the Huggenbergers. These Huggenberger indications were very small, from 3 to 31 microinches per inch. Due to their magnitude, the accuracy of these measurements is poor, and no correction

factors could be computed.

Table II

A-8 Strain Gage Correction Factors for 1,300 psi

Time, min.	Correction Factor
0	1.030
10	1.044
20	1.050
30	1.053
60	1.061
120	1.071
180	1.079

The error of the wire strain gages may be attributed to shear lag during the application of the load; in addition, stress relaxation of the Duco cement during the application of the load could have caused the cement to yield plastically so that the gages read high after removal of the load. The limited range of the Huggenbergers restricted the calibration to small strain; hence no other calibrations were made for larger loads. Instead, the results for 1300 psi were extrapolated, that is, Table II is used to correct the A-8 strain gage readings for all loads.

STRESS-STRAIN RELATION FOR CR-39

The stress divided by corrected strain is plotted as a function of time in Fig. 2. It can be seen that CR-39 is not linearly viscoelastic, since $\sigma/e_1 = f(t)$ for a linear viscoelastic material, where σ is the stress, e_1 is the strain, and t is time; but for CR-39, $\sigma/e_1 = f(t,\sigma)$. The values of strain have been interpolated from the original data; but the strain at zero time

cannot be extrapolated because strain readings were not made immediately after load application. However, the zero-time modulus can be calculated if the zero-time fringe order is known, as is shown later. Enough readings of the fringe order were made so that the zero-time fringe order could be extrapolated, and from this the calculated zero-time modulus of elasticity is 3.76×10^5 psi.

To demonstrate more clearly the nonlinearlity of CR-39, stress versus strain at 10 minutes after load application is shown in Fig. 3, for which the Young's modulus is 3.36×10^5 psi. Stress is based on original cross sectional area. It must be kept in mind that the usual range of A-8 wire strain gages is limited to strains less than 1%.

POISSON'S RATIO

For the simple tensile specimen, strain in the axial direction is plotted against strain in the transverse direction in Fig. 4. Poisson's ratio is given by the slope, which is 0.443.

OPTICAL BIREFRINGENCE OF CR-39

It is postulated that some transparent materials may be stress birefringent; that is, they follow the Maxwell law,

$$N = (\sigma_1 - \sigma_2)w/F \qquad (1)$$

where N is the fringe order, σ_1 and σ_2 are the principal stresses, w is the thickness of the specimen, and F is the stress-

fringe constant, which depends on the material and the wave length of the light.

On the other hand, a material may be strain birefringent and hence follow the Neumann law,

$$N = (e_1 - e_2)w/G \tag{2}$$

where e_1 and e_2 are the principal strains and G is the strain-fringe coefficient.

To be even more general, Coker and Filon (3) suggest that all transparent materials follow a linear combination of the Maxwell and Neumann relations.

Figure 1 clearly indicates that the fringe order depends on time as well as stress in a tensile specimen, and hence CR-39 does not follow the Maxwell relation. To determine whether or not CR-39 follows the Neumann relation, $e_1 - e_2$ is plotted against fringe order N in Fig. 5. N has been corrected for original thickness, and the strains have been corrected according to Table II. Values of $e_1 - e_2$ in excess of 1.44% may have exceeded the working range of the strain gages, and these points were not used to draw the line.

The strain-fringe constant, from Eq. (2) is given by

$$G = (e_1 - e_2)w/N \tag{3}$$

where $(e_1 - e_2)$ is given by the reciprocal of the slope of the line in Fig. 5, and $w = 0.252$ inches. Using these values, for CR-39

one gets for G:

$$G = 3.48 \times 10^{-4} \text{ in/fringe} \tag{4}$$

The stress fringe constant F(0) for zero time after load application can be determined by extrapolating the fringe order at zero time, N(0) from the creep tests. The zero-time fringe orders for the various loads have been plotted in Fig. 6 against stress multiplied by specimen thickness, and the slope of this curve gives F(0) since from Eq. (1),

$$F(t) = \sigma_1 w/N(t) \tag{5}$$

The value of F(0) is thus found to be 90.8 psi-in/fringe. E(0), the zero-time value of the elastic modulus can now be determined from Eq. (1) and (2), since

$$N(0) = \sigma_1 w/F(0) = [\, e_1(0) - e_2(0)] \, w/G. \tag{6}$$

Now, $e_1(0) - e_2(0) = (1 + \nu)e_1(0)$, and $\sigma_1 = E(0)e_1(0)$, where ν is Poisson's ratio; therefore:

$$E(0) = F(0)[1 + \nu]/G = \frac{(90.8)(1.443)}{3.48 \times 10^{-4}} = 3.76 \times 10^5 \text{ psi}$$

which is greater yet than E(10) which was found to be 3.36×10^5 psi from Fig. 3.

DISCUSSION OF STATIC TESTS

From the data, it is evident that for CR-39, the optical birefringence is directly proportional to the difference between principal strains up to and possibly beyond 18 fringe lines for

5461Å. On the other hand, CR-39 is definitely a non-linear viscoelastic plastic, for not only does the strain increase under load, but the rate of increase depends upon stress.

Referring to the method used by Coolidge, in which stress versus strain was determined from a tensile specimen by increasing the load every ten minutes; it is seen that the value of E, the elastic modulus, so obtained is good only for this method of loading and does not apply to photoelastic specimens to which the entire load is applied at once. These same comments apply to the method of determining the stress-fringe constant, since the time variable was not correctly controlled. Lastly, Coolidge determined optical creep from a beam subjected to pure bending, in which the total load was applied for 180 minutes. Since Fig. 3 indicates that CR-39 is not a linear viscoelastic plastic, stress is not proportional to strain in the beam and hence his method of calculating fiber stresses is not correct. In addition, each fiber of the beam cannot elongate individually according to time and the local stress as shown in Fig. 2; to the contrary, the longitudinal strain equals the distance from the neutral axis divided by the radius of curvature which is constant for all fibers so that stress relaxation must occur and hence the stress becomes even more non-linear over the depth of the beam.

The results of these static tests on CR-39 will serve for comparison with the dynamic values of Poisson's ratio,

the dynamic elastic modulus, and the dynamic strain-fringe constant.

DYNAMIC PROPERTIES OF CR-39

The suitability of any photoelastic plastic for the quantitative study of stress waves depends in a large part upon knowledge of the dynamic mechanical and birefringent properties. In this section, experiments and results will be described for the determination of Poisson's ratio, internal damping, and longitudinal stress wave speed as a function of frequency and wave length; and finally, the dynamic birefringent relations for CR-39.

DESCRIPTION OF DYNAMIC EQUIPMENT

The essential apparatus for these experiments is the dynamic loading frame, shown in Figs. 7 and 8. The frame has two tight wires in the vertical direction, one inch apart. An aluminum hammer slides on the wires, while a specimen rests on top of a steel anvil and is supported by two fixtures that clamp to the wires and which allow the specimen to slide vertically, but not laterally. In this way, the position of the face of the tests specimen relative to the hammer does not change between runs. The hammer is released from a set of jaws from the top of the frame by a small electromagnet. Just before the hammer strikes the specimen, it hits an

insulated portion of a thin steel wire, which in turn makes contact with another thin wire, closing the trigger circuit and starting the data recording devices. With care, the triggering is reproducible to within 10 microseconds for each run.

The velocity of the hammer at the time of impact was measured by removing the specimen and placing a lamp, thin slit, and photocell at the same height as the impact end of the specimen. As the hammer drops past the slit, the output of the photocell is recorded as two pips on an oscillograph. The velocity of fall is obtained by dividing the time between pips by the length of the hammer. The velocity of the hammer at impact for the setup of Fig. 7 was 222 inches /sec, ±1%.

Squareness of impact was obtained by placing a small rectangular piece of aluminum on top of the specimen, applying Duco cement to the top of this aluminum piece, and then bringing the hammer down into contact with the wet cement. Since the aluminum piece was in uniform contact with the specimen and, when the cement hardened, formed an integral part of the aluminum hammer; and since the wires maintain alignment between the hammer and specimen, square impact should be achieved. The completed hammer weighed 0.0360 lb.

To test for squareness of impact, a piece of carbon paper and tissue paper were placed on the impact end of the

specimen, and the hammer was released. The impact was fairly even, as shown by Fig. 9, which are records of the impact pressure that were made three months after the alignment process had been completed. As a final check, separate oscillograms of the output of the strain gages on both sides of the specimen were made for successive runs. The impacts were reproducible to within a few percent, as indicated by the similarity of oscillograms of the same strain gage. However, there was a definite difference between oscillograms of the outputs of the two strain gages, as shown in Figs. 10(a) and 10(b). These show that even with the precautions taken, square impact was still not achieved. However, if the outputs of the two strain gages are added, the average strain will be obtained without the bending strains, as shown in Fig. 10(c). Similarly, for an optical path through a small area on the center-line of the specimen, the average optical retardation will be obtained, unaffected by bending in the forward or backward direction. In all data reduction, the assumption is made that departures from a linear distribution of strain through the thickness of the specimen result in a second order effect and is therefore negligible. Since the gages and optical path are on the center-line of the specimen, they are unaffected by sideways bending.

Strain was detected by means of Type C-19 Baldwin wire strain gages, which were cemented to the specimen with Duco cement, which apparently had no effect on the CR-39 plastic. They were wired into a DC bridge that is essentially the same as that used by Ripperger (4). This bridge has the advantage

of subtracting out bending stresses. A calibrating resistor can be switched in parallel with one of the gages to calibrate the oscilloscope. The output of the bridge is connected to a Hewlett-Packard amplifier set at highest gain to reduce the amplifier noise, and from the output of the amplifier into an oscilloscope. Oscillograms were made by means of the Dumont-Land oscillograph camera. The frequency response of the amplifier and oscilloscope was checked and found to be flat in the range between 2 and 200 kilocycles. The rise time for a step input was found to be about 1.5 microseconds.

The specimen used for the Poisson ratio and birefringent dynamic tests was cut from a clear sheet of 0.248 inch thickness CR-39. Its length is 10.75 inches, and its width is 0.500 ±0.001 inches. Two C-19 strain gages were cemented on either side of the specimen in the longitudinal direction 4 inches below the impact end of the specimen, and two C-19 gages in the transverse direction 7/16 inch below the others. The gage constant given by the manufacturer was 2.51 ±3%.

DYNAMIC POISSON'S RATIO

For uniaxial stress, Poisson's ratio is equal to $-e_2/e_1$, where e_1 is the strain in the longitudinal direction and e_2 is the strain in the transverse direction. Oscillographs of e_1 during impact were made during a run, followed by another run during which a record of e_2 was made. Typical records are shown in Fig. 11. As can be seen, it is most convenient to

compare strains at the first or second peaks, which correspond to the initial wave and its reflection. The values of peak strain vary slightly from run to run, the largest difference being about 5% from the mean.

For the first peak, the average Poisson's ratio for 4 tests was 0.440. For the second peak, the average Poisson's ratio was 0.435 for 10 runs. In comparison with the static value, the dynamic Poisson's ratio is the same within experimental error. For the purpose of further calculations, a value of 0.44 ± 2% will be used.

WAVE SPEED, DYNAMIC ELASTIC MODULUS, AND DAMPING IN CR-39

In brief, it is desired to make experimental measurements that will determine the phase speed c of longitudinal sinusoidal stress waves, and the rate of their attenuation with distance. The experiments that are performed, however, determine the frequency and logarithmic decrement of free-free bars of CR-39 for longitudinal vibrations. Use is made of the theory of propagation of waves in solids having internal friction, which is covered quite completely in Kolsky (5); the following is an adaption of his discussion to these experiments.

If it is assumed that the material is a Voigt solid at any

one frequency, the stress-strain relation will be:

$$\sigma = E'e + E'' \frac{\partial e}{\partial t} \tag{7}$$

where σ and e are the stress and strain respectively in the axial direction of the bar and E' and E'' are constants. If the strains are varying sinusoidally with time, then:

$$e = e_o e^{i\omega t} \tag{8}$$

and Eq. (7) becomes:

$$\sigma = (E' + i\omega E'')e \tag{9}$$

where $e = \partial u/\partial x$. Therefore $E' + i\omega E''$ may be considered to be a complex elastic modulus, that is:

$$E^* = E' + i\omega E'' = E_1 + iE_2 = Ee^{i\varphi} \tag{10}$$

where

$$\left.\begin{aligned} E_1 &= E\cos\varphi \\ E_2 &= E\sin\varphi \\ \tan\varphi &= E_2/E_1 \end{aligned}\right\} \tag{11}$$

For longitudinal stress waves in a solid, if the wave lengths are long in comparison to the radius, Newton's law for an element becomes:

$$\rho \frac{\partial^2 u}{\partial t^2} = \frac{\partial \sigma}{\partial x} = Ee^{i\varphi} \frac{\partial^2 u}{\partial x^2} \tag{12}$$

where ρ is the mass per unit volume, and

where σ is given by Eq. (9) and (10). When a bar of length L is executing free-free longitudinal vibrations, for the first mode the displacement in the axial direction may be assumed to be:

$$u(x,t) = U(t) \sin \pi x/L . \tag{13}$$

Substituting for u(x,t), Eq. (12) becomes:

$$\frac{\partial^2 U(t)}{\partial t^2} + \frac{E}{\rho} e^{i\phi} \frac{\pi^2}{L^2} U(t) = 0, \tag{14}$$

for which the solution is:

$$U(t) = \cos\left\{\sqrt{\frac{E}{\rho}} \frac{\pi}{L} t \cos\frac{\phi}{2}\right\} e^{-\sin(\frac{\phi}{2})\sqrt{\frac{E}{\rho}}\frac{\pi}{L}t} \tag{15}$$

The frequency and period of oscillation are then:

$$f = \sqrt{\frac{E}{\rho}} \frac{1}{2L} \cos\frac{\phi}{2} \tag{16}$$

$$\tau = \sqrt{\frac{\rho}{E}} \frac{2L}{\cos\frac{\phi}{2}} . \tag{17}$$

while the wave length from Eq. (13) is:

$$\Lambda = 2L \tag{18}$$

and the speed of the waves is:

$$c = f\Lambda = \sqrt{\frac{E}{\rho}} \cos\frac{\phi}{2} . \tag{19}$$

The logarithmic decrement, defined as $\delta = \ln[u(t)/u(t+\tau)]$, for a total of n cycles is:

$$\delta = 2\pi \tan\frac{\varphi}{2} = \frac{1}{n} \ln \frac{u(t)}{u(t+\tau)}. \tag{20}$$

Hence for a given bar undergoing free-free vibrations, if measurements of the frequency and decay are made, δ, φ, c, E, E_1 and E_2 can be determined. However, one is also interested in the rate of decay of a given wave as it travels along a bar. For this purpose it may be assumed that:

$$u = U_1(x) \sin \omega t. \tag{21}$$

When this is substituted into the differential equation, Eq. (12) and it is solved, one gets:

$$U_1(x) = e^{i\sqrt{\frac{\rho}{E}}\,\omega \cos\frac{\varphi}{2}\,x} e^{-\sqrt{\frac{\rho}{E}}\,\omega \sin\frac{\varphi}{2}\,x} \tag{22}$$

The real negative coefficient of x may be called the attenuation factor α; and from Eq. (16) and (20)

$$\alpha = \delta/\Lambda \tag{23}$$

and the amplitude of a wave will decrease according to $e^{-\alpha x}$. If the logarithmic decrement is small, other simplifications may be made, for if $\tan\varphi \simeq \varphi$, from Eq. (11), (20) and (23),

$$\varphi = E_2/E_1 \tag{24}$$

$$\delta = \pi\varphi \tag{25}$$

$$\alpha = \pi E_2 / E_1 \tag{26}$$

and

$$E_1 = c^2 \rho . \tag{27}$$

Sometimes the "specific damping capacity" or "specific loss" is of interest. It is defined as the fractional change of energy in one cycle, and for small damping is given by:

$$\Delta W / W = 2\delta . \tag{28}$$

Experimental Procedure

Quarter-inch square rods of various length were placed in the dynamic loading frame shown in Fig. 7, and supported by a steel anvil on which sponge rubber had been placed. Two strain gages were cemented on opposite sides of the bars at the center; these were connected to an oscilloscope through the dynamic strain gage bridge. The hammer was then dropped, and an oscillograph record was made with the Dumont camera. After the initial transients died out, the bar vibrated freely in the first longitudinal mode, and the strain gages recorded the strain of the longitudinal vibrations.

For the shorter bars, a correction must be made for lateral motion of the bar. This is a correction to the wave speed c , and is analogous to the corrections for round bars discussed in Part V. The data for the correction has been taken from experiments by Morse (6) for square bars, and

a theoretical analysis by Bancroft (7). In computing the logarithmic decrement, strains were used instead of displacements, but this has no effect upon the results.

Experimental Results

Typical oscillograph records are shown in Fig. (12). The decay appears to be exponential, hence the previous analysis will be used to reduce the data. The results have been plotted in Figs. 13, 14 and 15. It is evident that the phase speed c only increases about 10% from wavelengths of 21.5 inches to 1.264 inches, but the absolute value of the elastic modulus increases over 20%. Furthermore, all values of the dynamic E are greater than any reported static values of E. The logarithmic decrement increases for shorter wave lengths, but the most striking increase with short wave length is the attenuation factor α, which increases about 27 times over the range that was investigated. Hence, the amplitude of a wave of 1.264 inch wave length will be reduced to 16% of its original amplitude in five inches. The experimental error for the frequency of vibration is about ±2%, and about ±10% for the logarithmic decrement.

The leading edge of the strain wave shown in Fig. 10(c) may now be interpreted in accordance with these results. The theoretical peak strain for that experiment was about 0.272%, but the measured peak strain was only 0.207%.

Moreover, the leading edge has a rise time of about 25 microseconds. These two effects are mostly due to the attenuation of the shorter wave length components of the leading edge of the wave, and to a lesser extent from internal reflections of the wave. A smaller effect is due to the finite length of the strain gage, which is discussed later.

It thus appears that CR-39 leaves much to be desired as a photoelastic plastic for impact experiments, because the phase speed of waves is not the same for all components, and the attenuation is too great.

DYNAMIC STRAIN-FRINGE CONSTANT

Introduction

Senior and Wells (8) measured the dynamic stress-fringe constant during the passage of a stress wave and found it to be about 60% higher than the static value for Xylonite. Their method consisted of shooting pellets at the end of a bar, and then taking one microsecond duration single flash photographs of the resulting fringe pattern, and then calculating the peak stress that would result if the impact were square, using the formula $\sigma = Ev/c$, where v is the particle velocity at the end of the bar, and c was assumed to be equal to $\sqrt{E/\rho}$, where ρ is the mass density of the plastic. As Flynn (9) has pointed out, these formulas

may not be applicable.

In 1954 Flynn (9) determined the dynamic stress-fringe constant for Castolite and Bakelite by taking slit photographs on a revolving-drum shutterless camera of the fringe pattern that resulted from a heavy mass hitting the end of a bar longitudinally. The fringe lines showed step-wise increases in accordance with the Boussinesq theory. Since the Boussinesq theory assumes that $c = \sqrt{E / \rho}$, and that $\sigma = Ev/c$, these two formulas were used, first to calculate the dynamic elastic modulus from the speed of the stress wave, and then to calculate the stress-fringe constant. He found that for Castolite, the dynamic and static elastic modulus was the same within experimental error, but that the dynamic stress-fringe constant was 27% higher than static. For Bakelite, the dynamic stress-fringe constant was found to be about 17% higher than static. However Flynn asserts that the Maxwell law applies to all materials, while his results are quite to the contrary. Furthermore, from his Fastax motion pictures, even with poor time resultion, it is evident that the impact was not square. Finally, Flynn recommends the use of strain gages and a ultra-high speed full frame motion picture camera, which is precisely the method evolved and used in this study.

Since CR-39 apparently follows the Neumann law for birefringence during creep tests; that is, the optical retardation is proportional to the difference between principal strains, it appears desirable to record simultaneously strain and optical retardation during the passage of a stress wave.

Experimental Procedure

The method for recording strain has previously been described, except that for this experiment only the strain in the longitudinal direction, e_1, is required, since $e_2 = -\nu e_1$. To record the optical birefringence, the loading frame was placed in a polariscope, shown in Fig. 16. Two slits 1/8 inch wide were placed on either side of the specimen, such that the light path passes between the longitudinal and transverse strain gages. The light source was a low pressure mercury vapor lamp, and a Wratten 77A filter was used to eliminate all wave lengths except the Hg green line 5461 Å. The intensity of transmitted light was detected by an RCA 1P21 multiplier phototube, the output of which was connected to a 514AD Tektronic oscilloscope.

The trigger circuit causes the 513D Tektronic oscilloscope to sweep and record the strain of the leading edge of the wave. The positive gate of this oscilloscope was connected to the trigger input of the 514AD so that both oscilloscopes swept

together. The delay trigger of the 513D oscilloscope was capacitance coupled to the input of both oscilloscopes so as to make a single coordinating timing mark. Two Dumont oscillograph cameras were used to obtain the oscillograph records, and a calibrated square wave generator was used to calibrate the sweep times of both oscilloscopes, which were set at about 5 microseconds per centimeter.

As before, the hammer weight was 0.0360 lb, and the impact velocity was 222 ±1% in/sec. The specimen is the same one as used for the Poisson's ratio tests.

Results

Two typical oscillograph records are reproduced in Fig. 17. They are for the leading edge of the stress wave, which has a rise time of about 25 microseconds. Oscillogram (a) is $2e_g$, that is, twice the recorded strain in the longitudinal direction; and (b) is the intensity of light transmitted through the specimen. The light intensity as shown in Fig. 17 (b) is related to the fringe order by

$$I(t) = I_o \sin^2 \pi N(t) \tag{29}$$

where I(t) is the instantaneous light intensity, I_o is the maximum light intensity, and N(t) is the instantaneous fringe order. Hence:

$$N(t) = \frac{1}{\pi} \sin^{-1} \sqrt{\frac{I(t)}{I_o}} \tag{30}$$

This is plotted as curve (c) in Fig. 17, and has a similar shape to curve (a) for strain. Finally, in Fig. 18 the number of fringe lines N is plotted vs. $(e_1 - e_2)w$ for eight runs, where $(e_1 - e_2)$ is calculated from:

$$(e_1 - e_2)w = (2e_g)(e_{cal})(1+\nu)w\,K/2e'_{cal} \qquad (31)$$

where:

$2e_g$ = ordinate of strain oscillograph in cm.

e_{cal} = resistor calibration strain = 0.3905×10^{-2} in/in.

ν = 0.44

w = thickness of specimen = 0.248 in.

K = correction factor for length of strain gage; see Appendix

e'_{cal} = ordinate in cm. of calibration line on oscillograph.

Therefore,

$$(e_1 - e_2)w = K(2e_{cal}) \times 0.697 \times 10^{-2}/e'_{cal} \qquad (32)$$

Figure 18 has been plotted in the following manner: From the time corresponding to that fringe order equal to one-half of the maximum fringe order on the leading edge of the stress wave, times were measured to integral and half-integral intensities; eg., to where $I = 0$, $I = 1/2\,I_o$, and $I = I_o$. The fringe order corresponding to each of these times was then computed from Eq. (30). For the same values of time

as measured from the strain corresponding to one-half maximum strain (allowing for the K factor), the ordinates of the strain oscillographs were measured. Then $(e_1 - e_2)w$ was computed for each ordinate from Eq. (31), and is plotted as the ordinate of Fig. 18 vs. the fringe order for the same times. As can be seen, the points fall close to a straight line. Unfortunately, the process of measuring times from the oscillograph records is somewhat inaccurate for two reasons: first, the time divisions themselves are rather minute and can be determined only to within about ±5%. Second, there seems to be some evidence that the oscilloscopes do not sweep with precisely the same speed each time. Therefore the strain-fringe constant was not determined from the slope of a straight line through the points. Instead, advantage was taken of the fact that the maximum strain of the leading edge of the wave, and the maximum fringe order could be determined to within ±3%. Therefore G was computed for each run as $(e_1 - e_2)_{max} w/N_{max}$, and G was averaged over eight runs. The result is:

$$G = 3.42 \times 10^{-4} \pm 3\% \text{ in/fringe.} \qquad (33)$$

The limitation in accuracy is primarily due to the C-19 Baldwin wire strain gages, and no way was found to calibrate them during transient straining. In comparison, the static value of G was found to be:

$$G_{static} = 3.48 \times 10^{-4} \pm 2\% \text{ in/fringe} \quad (4)$$

The difference between the two values is less than experimental error. It may be concluded that for dynamic strains of $e_1 - e_2$ less than 0.25×10^{-2} in/in, and strain rates up to 1.55×10^{-4} in/in per microsecond, the dynamic strain-optical law is the same as the static strain-optic law for CR-39.

Discussion

Referring to Flynn's experiments, it was found that for Bakelite, both the stress-fringe constant and the elastic modulus are greater for dynamic stresses than for static. For Castolite, the stress-fringe constant was found to be greater for dynamic stresses, but E was the same as static. However, the data for the dynamic elastic modulii are not conclusive, since they were based on the velocity of the leading edge of a stress wave, which actually propagates with the speeds of its Fourier components. A more desirable method is to determine E for sinusoidal waves of various wave lengths, as described previously.

The data demonstrates that for Bakelite, Castolite, and Xylonite, the Maxwell relation for stress birefringence is not valid over a large range of stress rates; but the data is inconclusive insofar as demonstrating strain birefringence. On the other hand, CR-39 seems to be strain birefringent

over a wide range of strain rates. In addition, Fried (10) found that polyethylene is strain birefringent in creep tests up to strains of 96%. Hence the Neumann law of strain birefringence has been demonstrated for two photoelastic plastics; but no materials have yet been found to follow Maxwell stress birefringence for all strain rates.

All of the foregoing tests were made at room temperature. It would be interesting to determine the variation of the strain-optic coefficient with temperature.

III ULTRA-HIGH SPEED PHOTOELASTIC MOTION PICTURES OF STRESS WAVES IN CR-39

Introduction

For a large number of plastics, stress waves propagate at a speed of about 60,000 inches per second. Consequently, in order to have a photographic resolution of at least 0.03 inches in the specimen, each photograph can not have an exposure time exceeding 0.6 microseconds. Therefore, early photoelastic motion pictures by Frocht (11), Tuzi and Nisida (12), and Murray (13) which had very long exposure times , while they showed time-varying stresses, did not show stress waves.

More recently, Shardin and Struth (14), Senior and Wells (7), and Christie (15) successfully photographed the isochromatics due to stress waves with a succession of single-flash photographs. Perkins (16) photographed the slower stress waves of photoelastic rubber at 5,000 frames per second, using a Fastax full frame motion picture camera.

Flynn (9) has taken slit photographs of stress waves using a revolving-drum camera. It should be noted that his claim of 1,500,000 frames per second is based on the reciprocal of the exposure time, but does not take into account lens resolution, focus, or film graininess. Examination of his drum camera photographic records revealsthat the time

resolution is more nearly 5 microseconds, or an equivalent of 200,000 frames per second. In his conclusion, Flynn recommends that an ultra-high speed full framing camera be used for recording transient isochromatics. He also has a very complete bibliography pertaining to dynamic photoelasticity and high speed motion picture techniques.

Photographic Techniques

In order to take motion pictures of the stress waves in photoelastic plastic, the camera that was developed by Dr. A. T. Ellis was utilized (17). Figure 19 shows the camera in position for photographing cavitation bubbles. This camera is a revolving mirror type; the mirror distributes a series of images onto the inner periphery of a stationary drum in which a 7-1/2 foot length of 35 mm. film has been placed. Eastman linograph pan film was used, and more recently a more sensitive film, Triple X, when it became available. The exposure time for each frame is achieved by a Kerr cell, which consists of a glass cell containing nitrobenzene. On the front and back of the cell are crossed Polaroids, so that normally, no light is transmitted through the cells. At right angles to the light path are two electrodes; when a voltage difference of 13,000 volts exists across these electrodes, the nitrobenzene becomes sufficiently optically active to rotate

the plane of polarization by 90^{o}, and the Kerr cell passes light. The Kerr cell was electrically pulsed for 10^{-7} seconds to achieve each frame. Repetition rates of up to 400,000 individual frames per second have been attained by reducing the time interval between electrical pulses to the Kerr cell and adjusting the rotational speed of the mirror. The Kerr cell is pulsed continuously during only one revolution of the mirror during which time a General Electric FT524 flash tube is illuminated by discharging through it the energy stored in a bank of capacitors. Suitable inductances cause the light intensity to be almost constant for about a millisecond. Figure 20 shows the mirror and air turbine.

Figure 21 is a schematic diagram showing the arrangement of the polariscope, specimen, and camera.

Experimental Results

Figure 22 shows four consecutive frames from an experiment in which the specimen was dropped onto a steel anvil. White light was used and the repitition rate was 20 microseconds between frames. Stress waves can be seen radiating from one corner of the specimen where contact with the anvil was first made. The dispersion of the wave front is also visible.

These frames demonstrate the feasibility of taking ultra-high speed photoelastic motion pictures of stress

waves. Using the experimentally determined values of the strain-fringe constant of CR-39, the difference in principal strains can be determined.

IV THE USE OF A MULTIPLIER PHOTOTUBE TO DETECT TRANSIENT STRAINS DUE TO CAVITATION

Introduction

Cavitation, as is well known, is that phenomenon associated with the growth and collapse of vapor bubbles in a liquid as it flows from a region in which the pressure is less than vapor pressure into a region of higher pressure. This process is usually accompanied by audible noise. Structural materials in the vicinity of the cavitation usually suffer severe damage in that the metal is gradually eaten away.

In order to study cavitation damage in the laboratory, Ellis has devised an acoustic method of creating cavitation (18). The essential apparatus is shown in Fig. 23, and consists of a glass beaker, a barium titinate ferroelectric ring surrounded by closed-cell sponge rubber, and a specimen holder, which in this case is a one-inch thick base of stainless steel. The specimen is held in the center of the base, and the beaker is filled with distilled and deaerated water. An audio-oscillator is connected to an amplifier whose output is then connected to the electrode surfaces of the barium titanate ring. When the audio-oscillator is tuned to the lowest resonant frequency of the system, the first mode of vibrations of the water-base-beaker system is excited. The maximum pressure amplitude in the beaker is on the center-

line near the base, and as the amplitude of oscillation is increased, the minimum pressure during the negative part of the cycle drops below vapor pressure, and cavitation can be started there. It takes the form of a small vapor bubble cloud on the upper end of the specimen.

Using this technique, Ellis and Plesset have subjected a great number of metals to cavitation for various lengths of time (19). The damage takes the form of pitting of the metal surface, but in addition, X-ray diffraction patterns have shown that the metal below the surface has become cold-worked. This cold-work increases with increased exposure and hard metals are generally more resistant to damage than softer ones.

Experimental Procedure

In order to determine the cause of this cold-work, a photoelastic specimen of CR-39, 1/16 x 1/16 x 1/8 in. was placed in the beaker, which was then placed in a polariscope. The light source is a General Electric AH-6 water cooled Hg lamp. A lens condenses the light into a beam which passes through the specimen and into an objective lens, so as to magnify the specimen eight times. A light slit, 1/32 in. square, could be moved about at the magnified image so that the fringe lines in an area 0.004 in. square on the specimen could be observed. To determine the light intensity passing through the slit, behind it was placed the 1P21 multiplier

phototube, enclosed in a double-wall vessel, with a vacuum between the walls. Liquid nitrogen was poured into the vessel to cool the phototube in order to reduce the noise. The phototube output was connected to a Tektronic type 121 amplifier and then into a type 513D Tektronic oscilloscope. The frequency response of the amplifier is 12 mc., and the oscilloscope 18 mc., according to the manufacturer. The frequency response of the phototube is at least as high as the oscilloscope, as determined by light pulse tests through a Kerr cell.

Experimental Results

The light slit was centered 0.006 in. below the upper surface of the CR-39 specimen. As the oscillator amplitude is increased, a distinct sine wave becomes visible on the oscilloscope screen, whose amplitude and frequency correspond to that of the oscillator. As the oscillator is tuned to the resonant frequency, 22 kc., the wave form of the light intensity becomes distorted from sinusoidal toward a sawtooth form. The bubble cloud forms, and a pip appears on the oscilloscope screen, at the part of the cycle where the pressure becomes positive. A typical oscillograph is shown in Fig. 24. The pips were present only when the bubble cloud was present. The bottom record, a double-exposure shows that the time between pips is not a constant. The time duration of the pip is about 2 microseconds. When

the slit is moved down away from the upper end of the specimen, the pips gradually decrease in amplitude.

Ultra-High Speed Motion Pictures of Cavitation Stresses.

Using a slightly different cavitation beaker with a resonant frequency of 10 kc., ultra-high speed motion pictures were taken of the bubble cloud and photoelastic specimen. A typical cycle is shown in Fig. 25. The specimen was 1/4 inch thick; its edge is the black line nearest the bubbles. The next two black lines are time-edge isochromatics, caused by leaving the specimen immersed in water. These isochromatics are very sensitive; their displacement indicates the presence of strains.

The cycle starts when the pressure drops below vapor pressure, causing many small vapor bubbles to form, as in Frame 1. As the pressure decreases, the bubbles continue to grow, until the pressure starts to increase, at which time they begin to collapse. The last bubbles appear as a black cloud in Frame 11. In Frame 12, the time-edge isochromatics have become displaced, and the entire portion of the specimen in field of view has become darkened, especially near the bubbles. The bubbles in Frames 12 to 15 are rebound bubbles, which proceed also to collapse until no vapor bubbles are present, at which time the next cycle begins. Thus, the collapse of vapor bubbles is accompanied by strains in the vicinity of the last bubbles. To refine this technique and interpret the pictures, further tests are planned.

V ANALYSIS OF LONGITUDINAL STRESS WAVES IN BARS

Introduction

Most of the experiments that are described in the previous sections involve longitudinal impacts of bars, and most investigators have sought a theory of impact to compare to their experiments. The exact theory of longitudinal stress waves in round bars as developed by Pochhammer (20), and in rectangular bars by Morse (21), were developed from the exact equations of elasticity by assuming that the particle displacements in the bar vary sinusoidally with time, while the lateral boundary remained free of stress. This leads to a solution which contains an infinite number of radial modes, and hence has not been found suitable for solving problems of impact (32). This has led to a number of attempts to derive more usable approximate solutions. These involve assuming the radial variations of the strains and then solving for the remainder. The general procedure can be described by saying that the axial displacement u, and the radial displacement v of a particle at distance r from the centerline of the bar should have the following form:

$$u = u_1 + u_2 F_2(r) + u_3 F_3(r) + \cdots \tag{34}$$

$$v = v_1 f_1(r) + v_2 f_2(r) + v_3 f_3(r) + \cdots \tag{35}$$

where the u_n and v_n are functions of the distance along the bar x, and time t. The $f_n(r)$ are related to the radial modes of vibration in the bar and the $F_n(r)$ are related to the $f_n(r)$ in such a manner so that for sufficiently long wave length stress waves that are

propagating along the bar the u displacements are plane waves, and for sufficiently short wave lengths they are surface waves.

The zero order approximation is obtained by taking all of the v_n and u_n except u_1 equal to zero which leads to the equation of motion

$$E \frac{\partial^2 u}{\partial x^2} = \rho \frac{\partial^2 u}{\partial t^2} \tag{36}$$

where E is the elastic modulus and ρ is the mass density. The velocity of propagation is given by $c_o = \sqrt{E/\rho}$. This simplest equation does not predict wave dispersion. Further efforts were directed toward establishing an intermediate theory between Eq.(36) and the exact theory.

The first order of approximation, $v_1 = \partial u/\partial x$; $f_1(r) = -\nu r$; and $u_n = v_n = 0$ for $n > 1$ was used by Rayleigh(22) to deduce the influence of radial inertia only, from which Love obtained the following equation of motion (23):

$$\frac{\partial^2 u}{\partial x^2} - \frac{1}{c_o^2} \frac{\partial^2 u}{\partial t^2} + \frac{\nu^2 k^2}{c_o^2} \frac{\partial^4 u}{\partial x^2 \partial t^2} \tag{37}$$

where ν is Poisson's ratio and k is the polar radius of gyration of the cross-section of the bar, which gives the following expression for the velocity of sinusoidal waves in a round bar of radius a:

$$c = c_o / \sqrt{1 + 2\pi^2 \nu^2 a^2 / \Lambda^2} \tag{38}$$

where Λ is the wave length.

Equation (38) is plotted as Curve II of Fig. 26 where it is seen that the phase speed goes to zero for shorter wavelengths, which is not in accordance with either the exact theory shown by Curve I, nor with experimental measurements made by Morse (24).

Mindlin and Herrmann (25) analyzed a higher approximation by taking $f_1(r) = r/a$; $v_1 = v_1(x,t)$; and $u_n = v_n = 0$ for $n > 1$. This introduced the first radial mode into the analysis and leads to a pair of differential equations in u and v_1, or when v_1 is eliminated, to an equation of fourth order in u.

It appears that any higher order approximations involving the second or third radial modes lead to differential equations of motion that are too complicated to lend themselves to analysis of specific problems. The differential equation of Mindlin and Herrmann is already in a form which makes analysis extremely difficult. The differential equation of Love is of relatively simple form but does not contain as many pertinent physical characteristics as that of Mindlin and Herrmann. In fact the equation of Love does not contain all of the physical information implied by taking $v_1 f_1(r) = -(\partial u/\partial x)\nu r$. It is the purpose of this section to examine the full implication of this first order approximation. It will be noted that any approximation which includes only a finite number of terms in u and v cannot satisfy the conditions that the sides of the bar be stress-free, nor can it give a good approximation to the stress

distribution for very short wave lengths.

One-Dimensional Equations of Motion

The Rayleigh assumptions are that:

$$u = u(x,t) \tag{39}$$

$$v = -\nu r \frac{\partial u}{\partial x}. \tag{40}$$

Using Hooke's law it is found that $\sigma_\theta = \sigma_r = 0$ and that $\sigma_x = E\partial u/\partial x$, where σ_θ is the circumferential stress, σ_r is the radial stress, and σ_x is the axial stress. The strain energy of extension, dV_1, in a small volume $dA\,dx$, where dA is a small element of cross section, is:

$$dV_1 = \frac{1}{2}(\sigma_x e_x + \sigma_r e_r + \sigma_\theta e_\theta)\,dA\,dx. \tag{41}$$

Equation (41) is next integrated over the entire length 2L of the bar to get:

$$V_1 = \frac{1}{2} EA \int_{-L}^{L} \left(\frac{\partial u}{\partial x}\right)^2 dx. \tag{42}$$

Using Eq.(40), the shear strain, γ_{xr}, is given by:

$$\gamma_{xr} = \frac{\partial v}{\partial x} + \frac{\partial u}{\partial r} = -\nu r \frac{\partial^2 u}{\partial x^2} \tag{43}$$

from which the shear strain energy, V_2, is:

$$V_2 = \frac{1}{2}\int_{-L}^{L}\int_{A} \tau_{xr}\gamma_{xr}\,dA\,dx = \frac{G}{2}\int_{-L}^{L}\int_{A} \nu^2 r^2 \left(\frac{\partial^2 u}{\partial x^2}\right) dA\,dx. \tag{44}$$

Equation (44) is next integrated over the cross section to obtain :

$$V_2 = \frac{1}{2} GA\nu^2 k^2 \int_{-L}^{L} \left(\frac{\partial^2 u}{\partial x^2}\right) dx. \tag{45}$$

Neither Rayleigh nor Love included this term in their theory. The kinetic energy of longitudinal motion, T_1, is:

$$T_1 = \frac{\rho}{2}\int_{-L}^{L}\int_{A}\left(\frac{\partial u}{\partial t}\right)^2 dA\,dx = \frac{\rho A}{2}\int_{-L}^{L}\left(\frac{\partial u}{\partial t}\right)^2 dx \tag{46}$$

The kinetic energy of lateral motion, T_2, is then:

$$T_2 = \frac{\rho}{2}\int_{-L}^{L}\int_{A}\left(\frac{\partial v}{\partial t}\right)^2 dA\,dx = \frac{1}{2}\rho A v^2 k^2\int_{-L}^{L}\left(\frac{\partial^2 u}{\partial t\,\partial x}\right)^2 dx \tag{47}$$

From Hamilton's principle, the variation equation of motion is:

$$\delta\int_{0}^{t}(T-V)\,dt = \delta\int_{0}^{t}(T_1+T_2-V_1-V_2)\,dt = 0 \tag{48}$$

Substitution of Eq. (42), (45), (46), and (47) into Eq. (48) gives:

$$\delta\int_{0}^{t}dt\int_{-L}^{+L}dx\left\{\frac{\rho A}{2}\left(\frac{\partial u}{\partial t}\right)^2 + \frac{\rho A v^2 k^2}{2}\left(\frac{\partial^2 u}{\partial t\,\partial x}\right)^2 - \frac{EA}{2}\left(\frac{\partial u}{\partial x}\right)^2 - \frac{GAv^2k^2}{2}\left(\frac{\partial^2 u}{\partial x^2}\right)^2\right\} = 0 \tag{49}$$

The terms in Eq. (49) are next integrated by parts as follows:

$$\delta\int_{0}^{t}\left(\frac{\partial u}{\partial t}\right)^2 dt = 2\int_{0}^{t}\frac{\partial u}{\partial t}\,\frac{\partial \delta u}{\partial t}\,dt = 2\frac{\partial u}{\partial t}\,\delta u\Big|_{0}^{t} - 2\int_{0}^{t}\frac{\partial^2 u}{\partial t^2}\,\delta u\,dt \tag{49a}$$

$$\delta\int_{0}^{t}\int_{-L}^{L}\left(\frac{\partial^2 u}{\partial t\,\partial x}\right)^2 dt\,dx = 2\int_{0}^{t}\int_{-L}^{L}\frac{\partial^2 u}{\partial t\,\partial x}\,\frac{\partial^2 \delta u}{\partial t\,\partial x}\,dt\,dx = 2\int_{-L}^{L}\frac{\partial^2 u}{\partial t\,\partial x}\,\frac{\partial \delta u}{\partial x}\Big|_{0}^{t}dx$$
$$-2\int_{0}^{t}\frac{\partial^3 u}{\partial t^2\,\partial x}\,\delta u\Big|_{-L}^{L}dt + 2\int_{0}^{t}\int_{-L}^{L}\frac{\partial^4 u}{\partial t^2\,\partial u^2}\,\delta u\,dt\,dx \tag{49b}$$

$$\delta\int_{-L}^{L}\left(\frac{\partial u}{\partial x}\right)^2 dx = 2\frac{\partial u}{\partial x}\,\delta u\Big|_{-L}^{L} - 2\int_{-L}^{L}\frac{\partial^2 u}{\partial x^2}\,\delta u\,dx \tag{49c}$$

$$\delta\int_{-L}^{L}\left(\frac{\partial^2 u}{\partial x^2}\right)^2 dx = 2\frac{\partial^2 u}{\partial x^2}\,\frac{\partial \delta u}{\partial x}\Big|_{-L}^{L} - 2\frac{\partial^3 u}{\partial x^3}\,\delta u\Big|_{-L}^{L} + 2\int_{-L}^{L}\frac{\partial^4 u}{\partial x^4}\,\delta u\,dx \tag{49d}$$

The integrated terms are then assumed to be zero, and the indicated substitutions are made into Eq. (49). The equation is satisfied if the coefficient of δu is zero, which leads to the following differential equation of axial motion:

$$-\rho\frac{\partial^2 u}{\partial t^2} + E\frac{\partial^2 u}{\partial x^2} + \rho\nu^2 k^2\frac{\partial^4 u}{\partial t^2 \partial x^2} - G\nu^2 k^2\frac{\partial^4 u}{\partial x^4} = 0 \quad (50)$$

which is the same as the Rayleigh-Love theory, Eq. (37), except for the additional term containing G.

One-Dimensional Sinusoidal Stress Waves

Since the dependence of the phase speed c on wave length Λ is of interest for comparison to other theories, consider the following wave:

$$u = D\sin\frac{2\pi}{\Lambda}(x - ct) \quad (51)$$

where D is the amplitude of motion. If this is substituted into the differential equation, Eq.(50), there is obtained:

$$\rho c^2 + \rho c^2\nu^2 k^2\left(\frac{2\pi}{\Lambda}\right)^2 - E - G\nu^2 k^2\left(\frac{2\pi}{\Lambda}\right)^2 = 0. \quad (52)$$

Since $G = E/2(1+\nu)$, and for a round bar $k^2 = a^2/2$, this gives:

$$c = c_o\sqrt{\frac{1 + \frac{\nu^2\pi^2}{1+\nu}\left(\frac{a}{\Lambda}\right)^2}{1 + 2\nu^2\pi^2\left(\frac{a}{\Lambda}\right)^2}}. \quad (53)$$

Curve III of Fig.26 is a plot of Eq.(53) for $\nu = 0.29$. The asymptotic value of c as a/Λ approaches infinity is $0.621\,c_o$, which is equal to the velocity of distortional waves in isotropic media, whereas it should be the velocity of Rayleigh surface waves, which for $\nu = 0.29$ is $0.5764\,c_o$ (26).

This discrepancy arises from the imposed condition that plane sections remain plane.

In comparison, the equation that Mindlin and Herrmann obtained is:

$$-\rho\frac{\partial^2 u}{\partial t^2} + E\frac{\partial^2 u}{\partial x^2} + \frac{3-4\nu}{4}\rho k^2\frac{\partial^4 u}{\partial t^2 \partial x^2} - \frac{1-\nu}{2}Gk^2\frac{\partial^4 u}{\partial x^4} - \frac{1-2\nu}{4}\frac{\rho k^2}{G}\frac{\partial^4 u}{\partial t^4} = 0. \qquad (54)$$

The phase velocity of sinusoidal waves given by this equation is shown as Curve IV in Fig.26 . The assumptions on which Eq. (54) is based rule out the possibility of correct stress distributions for short wave lengths; in particular the assumptions cause sizable shear stresses on the surface of the bar. To counteract this, Mindlin and Herrmann proposed modifying the coefficients in Eq. (54) to obtain a closer agreement to Curve I. This could also be done with Eq. (50), to bring Curve III into closer agreement with Curve I. It will be noted that Eq. (54) differs from Eq. (50) essentially only in the extra term containing the fourth time derivative. This term, however, makes Eq. (54) more difficult to solve than Eq. (50).

Characteristic Velocities

It is desirable to know whether or not Eq. (50) is a wave equation. This can be accomplished by transforming the equation from x - t coordinates to φ-ψ characteristic coordinates. In the theory of characteristics (27), initial conditions cannot be

specified on a characteristic; in addition, discontinuities may propagate along a characteristic. Now, along a given characteristic φ,

$$d\varphi = 0 = \frac{\partial \varphi}{\partial t} dt + \frac{\partial \varphi}{\partial x} dx \tag{55}$$

Hence,

$$\frac{dt}{dx} = - \frac{\frac{\partial \varphi}{\partial x}}{\frac{\partial \varphi}{\partial t}} \tag{56}$$

Computing the derivatives,

$$\begin{aligned}
\frac{\partial u}{\partial x} &= \frac{\partial u}{\partial \varphi} \frac{\partial \varphi}{\partial x} + \frac{\partial u}{\partial \psi} \frac{\partial \psi}{\partial x} \\
\frac{\partial^2 u}{\partial x^2} &= \frac{\partial^2 u}{\partial \varphi^2}\left(\frac{\partial \varphi}{\partial x}\right)^2 + 2\frac{\partial^2 u}{\partial \varphi \partial \psi} \frac{\partial \varphi}{\partial x} \frac{\partial \psi}{\partial x} + \frac{\partial^2 u}{\partial \psi^2}\left(\frac{\partial \psi}{\partial x}\right)^2 + \frac{\partial u}{\partial \varphi} \frac{\partial^2 \varphi}{\partial x^2} + \frac{\partial u}{\partial \psi} \frac{\partial^2 \psi}{\partial x^2} \\
&\cdots\cdots \\
\frac{\partial^4 u}{\partial x^4} &= \frac{\partial^4 u}{\partial \varphi^4}\left(\frac{\partial \varphi}{\partial x}\right)^4 + \cdots \\
\frac{\partial^4 u}{\partial t^2 \partial x^2} &= \frac{\partial^4 u}{\partial \varphi^4}\left(\frac{\partial \varphi}{\partial t}\right)^2\left(\frac{\partial \varphi}{\partial x}\right)^2 + \cdots
\end{aligned} \tag{57}$$

By substitution of the derivatives of u into Eq. (50) from Eq. (57), the following is obtained:

$$\left[\rho \nu^2 k^2 \left(\frac{\partial \varphi}{\partial x}\right)^2 \left(\frac{\partial \varphi}{\partial t}\right)^2 - G \nu^2 k^2 \left(\frac{\partial \varphi}{\partial x}\right)^4\right] \frac{\partial^4 u}{\partial \varphi^4} + \cdots = 0. \tag{58}$$

The solution of Eq. (58) is indeterminate if the coefficient of $\frac{\partial^4 u}{\partial \varphi^4}$ is zero. Hence the equation of a characteristic, after substituting from Eq. (56) and simplifying, is:

$$\rho\left(\frac{dt}{dx}\right)^2 - G\left(\frac{dt}{dx}\right)^4 = 0. \tag{59}$$

The above equation has four characteristics:

$$\frac{dx}{dt} = \pm\infty \,, \tag{60a}$$

$$\frac{dx}{dt} = \pm\sqrt{\frac{G}{\rho}} \,. \tag{60b}$$

Therefore, there exists only one characteristic speed, that of Eq. (60b). The speed of infinity is similar to that obtained from a diffusion differential equation. Hence the approximate differential equation, Eq. (50), for axial motion of a bar is partly a diffusion equation and partly a wave equation. It should be noted that the same results as Eqs. (60a) and (60b) can be obtained by taking the Laplace transform of Eq. (50); for if the inversion formula for large p is of a form

$$u = \frac{1}{2\pi i}\int_{\alpha - i\infty}^{\alpha + i\infty} f(p)\, e^{p(t - x/c)}\, dp \tag{61}$$

then the characteristic velocities are represented by c. In comparison, the exact theory gives the Rayleigh surface wave velocity as the speed of short waves in the first radial mode, and the distortional velocity for the second radial mode.

Propagation of Longitudinal Stress Waves Due to a Concentrated Disturbance at the End of a Bar.

Consider a semi-infinite bar for which $0 < x < \infty$. The bar is initially undisturbed; that is:

$$u(x, 0) = 0 \tag{62}$$

and there are no disturbances at infinity; that is:

$$u(\infty, t) = \frac{\partial u}{\partial x}(\infty, t) = \frac{\partial u}{\partial t}(\infty, t) = \cdots = 0. \tag{63}$$

The problem of impact at the end of the bar is first solved using Eq. (36), the simplest theory for the case of rigid mass m with a velocity v_o striking the end of the bar. It may easily be shown that the induced velocities in the bar are:

$$\begin{aligned} \frac{\partial u}{\partial t}(x, t) &= v_o e^{\frac{AE}{mc_o^2}(x - c_o t)}, \quad t > x/c_o; \\ \frac{\partial u}{\partial t}(x, t) &= 0, \quad t < x/c_o. \end{aligned} \tag{64}$$

Next let $m \to 0$ in such a manner that the product $v_o m$ remains finite, to obtain the result that if $t = x/c_o$ then $\partial u/\partial t = \infty$, but if $t \neq x/c_o$ then $\partial u/\partial t = 0$. Hence $\partial u/\partial t$ is given by

$$\frac{\partial u}{\partial t} = -c_o h\, \delta\left(\frac{x}{a} - \frac{c_o t}{a}\right) = a c_o h\, \delta(x - c_o t) \tag{65}$$

where h is the dimensionless strength of the impact, which may be determined by integrating Eqs. (64) and (65) with respect to time and equating the two results, giving:

$$h = \frac{v_o m c_o}{AEa}. \tag{66}$$

The initial conditions at $t = 0$ for the Boussinesq theory are:

$$u(x, 0) = 0; \quad \frac{\partial u}{\partial t}(x, 0) = -a c_o h\, \delta(x). \tag{67}$$

In addition, it is postulated that the end of the bar at $x = 0$ is

free after impact so that:

$$\frac{\partial u}{\partial t}(0,t) = 0. \tag{68}$$

Next, Eq. (50), the intermediate theory is solved for the same initial conditions by utilizing the Fourier cosine transform pair:

$$\left.\begin{aligned} \breve{u}(\kappa,t) &= \frac{1}{\pi}\int_0^\infty u(x,t)\cos\kappa x\,dx \\ u(x,t) &= 2\int_0^\infty \breve{u}(\kappa,t)\cos\kappa x\,d\kappa \end{aligned}\right\} \tag{69}$$

where κ can be considered as 2π times the wave number; that is:

$$\kappa = 2\pi/\Lambda. \tag{70}$$

Equation (50) is next multiplied by $(1/\pi)\cos\kappa x$ and integrated from $x = 0$ to $x = \infty$ to obtain:

$$-\frac{\rho}{\pi}\int_0^\infty \frac{\partial^2 u}{\partial t^2}\cos\kappa x\,dx + \frac{\rho\nu^2\kappa^2}{\pi}\int_0^\infty \frac{\partial^4 u}{\partial t^2\partial x^2}\cos\kappa x\,dx + \frac{E}{\pi}\int_0^\infty \frac{\partial^2 u}{\partial x^2}\cos\kappa x\,dx - \frac{G\nu^2\kappa^2}{\pi}\int_0^\infty \frac{\partial^4 u}{\partial x^4}\cos\kappa x\,dx = 0. \tag{71}$$

Since $\cos\kappa x$ is not a funtion of t,

$$-\frac{\rho}{\pi}\frac{\partial^2}{\partial t^2}\int_0^\infty u\cos\kappa x\,dx + \frac{\rho\nu^2\kappa^2}{\pi}\frac{\partial^2}{\partial t^2}\int_0^\infty \frac{\partial^2 u}{\partial x^2}\cos\kappa x\,dx + \frac{E}{\pi}\int_0^\infty \frac{\partial^2 u}{\partial x^2}\cos\kappa x\,dx - \frac{G\nu^2\kappa^2}{\pi}\int_0^\infty \frac{\partial^4 u}{\partial x^4}\cos\kappa x\,dx = 0. \tag{72}$$

Next, the terms involving derivatives of u are integrated by parts to obtain:

$$\int_0^\infty \frac{\partial^2 u}{\partial x^2}\cos\kappa x\,dx = \frac{\partial u}{\partial x}\cos\kappa x\Big|_0^\infty + \kappa\int_0^\infty \frac{\partial u}{\partial x}\sin\kappa x\,dx. \tag{73}$$

The integrated term, from Eq.(68) is zero. Equation (73) is integrated by parts again to obtain:

$$\int_0^\infty \frac{\partial^2 u}{\partial x^2} \cos \kappa x \, dx = -\kappa^2 \int_0^\infty u \cos \kappa x \, dx. \tag{74}$$

Similarly,

$$\int_0^\infty \frac{\partial^4 u}{\partial x^4} \cos \kappa x \, dx = -\kappa^4 \int_0^\infty u \cos \kappa x \, dx. \tag{75}$$

Equation (72) then becomes:

$$\frac{\rho}{\pi} \frac{\partial^2}{\partial t^2} \int_0^\infty u \cos \kappa x \, dx + \frac{\rho \nu^2 k^2 \kappa^2}{\pi} \int_0^\infty u \cos \kappa x \, dx + \frac{E \kappa^2}{\pi} \int_0^\infty u \cos \kappa x \, dx + \frac{G \nu^2 k^2 \kappa^4}{\pi} \int_0^\infty u \cos \kappa x \, dx = 0. \tag{76}$$

Then substitute from Eq.(69) for the Fourier transform to obtain:

$$\rho \frac{\partial^2 \breve{u}}{\partial t^2} + \rho \nu^2 k^2 \kappa^2 \frac{\partial^2 \breve{u}}{\partial t^2} + E \kappa^2 \breve{u} + G \nu^2 k^2 \kappa^4 \breve{u} = 0 \tag{77}$$

or, rearranging,

$$\frac{\partial^2 \breve{u}}{\partial t^2} + \omega^2 \breve{u} = 0 \tag{78}$$

where:

$$\omega^2 = \frac{E}{\rho} \left(\frac{\kappa^2 + \frac{\nu^2 a^2 \kappa^2}{4(1+\nu)}}{1 + \frac{\nu^2 a^2 \kappa^2}{2}} \right) \tag{79}$$

since $G = E/2(1+\nu)$ and $k^2 = a^2/2$ for a round bar. The solution of Eq. (78) is:

$$\breve{u} = B_1 \sin \omega t + B_2 \cos \omega t \tag{80}$$

for which the initial conditions at t = 0 are:

$$\left.\begin{aligned} \breve{u}(o) &= B_2 = \frac{1}{\pi}\int_o^\infty u(x,o)\cos\kappa x\,dx = o. \\ \frac{\partial \breve{u}}{\partial t}(o) &= \omega B_1 = -\frac{ac_o h}{\pi}\int_o^\infty \delta(x)\cos\kappa x dx = -\frac{ac_o h}{\pi}. \end{aligned}\right\} \tag{81}$$

Hence Eq. (80) becomes:

$$\breve{u} = -\frac{ac_o h}{\pi\omega}\sin\omega t. \tag{82}$$

From the inverse transform of Eq. (69),

$$u = -\frac{2ac_o h}{\pi}\int_o^\infty \sin\omega t\cos\kappa x\,\frac{d\kappa}{\omega}. \tag{83}$$

Using DeMoivre's theorem, Eq. (83) becomes:

$$u = -\frac{ac_o h}{2\pi i}\left[\int_{-\infty}^{\infty} e^{i(\omega t+\kappa x)}\frac{d\kappa}{\omega} + \int_{-\infty}^{\infty} e^{i(\omega t-\kappa x)}\frac{d\kappa}{\omega}\right]. \tag{84}$$

The first term represents waves travelling in the negative x direction; the second represents waves travelling in the positive x direction; hence it is only necessary to integrate the second term. This can be integrated approximately by the method of stationary phase (28), giving the result:

$$\begin{aligned} u = -\frac{ac_o h\sqrt{2\pi}}{2\pi i\sqrt{\left|t\,\frac{\partial^2\omega}{\partial\kappa^2}(\kappa_o)\right|}\,\omega(\kappa_o)}\Big\{ & e^{i\left[\omega(\kappa_o)t - \kappa_o x + \frac{\pi}{4}\operatorname{sgn}\frac{\partial^2\omega}{\partial\kappa^2}(\kappa_o)\right.} \\ & - e^{-i\left[\omega(\kappa_o)t - \kappa_o x + \frac{\pi}{4}\operatorname{sgn}\frac{\partial^2\omega}{\partial\kappa^2}(\kappa_o)\right]}\Big\}. \end{aligned} \tag{85}$$

The second term in the bracket arises from the fact that there are two points of stationary phase; one each for $+K_o$ and $-K_o$. Equation (85) when simplified becomes:

$$u = -\frac{a c_0 h\sqrt{2/\pi}}{\omega(\kappa_0)\sqrt{t\left|\frac{\partial^2\omega}{\partial\kappa^2}(\kappa_0)\right|}} \sin\left[\omega(\kappa_0)t - \kappa_0 x + \frac{\pi}{4}\,\mathrm{sgn}\frac{\partial^2\omega}{\partial\kappa^2}(\kappa_0)\right] \tag{86}$$

where κ_0, the point of stationary phase, is determined by the condition:

$$\frac{\partial\omega}{\partial\kappa}(\kappa_0) = \frac{x}{t}. \tag{87}$$

To simplify the calculations, the following substitutions are used to make Eq. (87) dimensionless:

$$\left.\begin{aligned} x &= \xi a\sqrt{\frac{\nu^2}{4(1+\nu)}} \\ t &= \tau_1 \frac{a}{c_0}\sqrt{\frac{\nu^2}{4(1+\nu)}} \\ u &= U a h\sqrt{2/\pi} \\ \kappa_0 &= \frac{X}{a}\sqrt{\frac{4(1+\nu)}{\nu^2}} \\ \omega &= V\frac{c_0}{a}\sqrt{\frac{4(1+\nu)}{\nu^2}} \\ \frac{\partial^2\omega}{\partial\kappa^2} &= Y a c_0\sqrt{\frac{\nu^2}{4(1+\nu)}} \\ Z &= \xi/\tau_1 \end{aligned}\right\} \tag{88}$$

Using these subsitutions, Eq. (87) becomes:

$$U = -\frac{\sin\left[\tau_1(V - XZ) + \frac{\pi}{4}\,\mathrm{sgn}\frac{\partial^2\omega}{\partial\kappa^2}(\kappa_0)\right]}{V\sqrt{\tau_1|Y|}}. \tag{89}$$

For $\nu = 0.5$, the following relations are obtained:

$$Z = \frac{1 + 2X^2 + 3X^4}{(1+X^2)^{1/2}(1+3X^2)^{3/2}} \tag{90}$$

$$V = \frac{X(1+X^2)^{1/2}}{(1+3X^2)^{3/2}} \tag{91}$$

and

$$Y = X\left\{\frac{4+12X^2}{(1+X^2)^{1/2}(1+3X^2)^{3/2}} - \frac{Z(10+12X^2)}{(1+X^2)(1+3X^2)}\right\}. \tag{92}$$

Z, Y, and V were calculated for various values of X. Hence to find U at a particular value of t and x, Eqs.(88) are used to calculate ξ, τ_1, and then Z. From the tabulations, the corresponding value of X is selected, then for that value of X, Y and V are found from the calculated tables. Finally, U is calculated from Eq.(89). These calculations were made for $\nu = 0.5$ and $\xi = 100$ (that is, $x = 20.412\,a$). Figure 27 is a plot of U vs τ_1. The solution predicts an initial disturbance, which is shown dotted, as its shape is not given by Eq.(89) according to Lamb's criterion for the method of stationary phase. At a later time a disturbance travelling at the shear velocity appears. Lamb's criterion is:

$$\frac{\partial^3\omega}{\partial k^3}(k_0)t \Big/ \left[\frac{\partial^2\omega}{\partial k^2}(k_0)\right]^{3/2} t^{3/2} \ll 1 \tag{93}$$

or in terms of the dimensionless variables,

$$\frac{\partial Y/\partial X}{\tau_1^{1/2}|Y|^{3/2}} \ll 1. \tag{94}$$

For the wave of Fig.27, $Y = 0$ near the wave front, and hence Eq.(89) does not hold there. But when $\tau_1 = 107$, Y is finite, and $\partial Y/\partial X = 0$. The only other zero of Y is near $\tau_1 = 190$. Thus Eq.(89) appears to be the valid solution from $\tau_1 = 107$ to about $\tau_1 = 188$. For values of τ_1 greater than 188 and less

than 107, the solution is not reliable.

It is of interest to compare Eq.(89) with the simple theory solution, which is:

$$\left.\begin{aligned} U &= \frac{u}{ah\sqrt{2/\pi}} = 1.253 \qquad t > x/c_o \\ U &= 0 \qquad t < x/c_o . \end{aligned}\right\} \tag{95}$$

For dispersive wave systems, energy travels with the group velocity, which is given by $\partial\omega/\partial\kappa$. From Eq.(87) this is just x/t. For a given group velocity, $\partial\omega/\partial\kappa$ is a function of κ_o only, hence κ_o is a constant. From Eq.(70) it is seen that the wave lengths of waves travelling with each group velocity are constant. But the phase velocity for a given wavelength is greater than the group velocity; hence as the wave of Eq.(89) travels along the bar, the individual waves move toward the wave front, increasing in wavelength.

The shortest waves are propagated with group velocities equal to $\sqrt{G/\rho}$ and form a discontinuity which is represented schematically in Fig.27 . However, a/λ is large for these waves, and Eq.(89) then does not give quantitatively correct results because of the assumption of plane sections.

Experimental measurements of the strain at a point on a bar impacted at one end have been made by Petersson using wire strain gages (29). His experimental records indicate an initial disturbance followed by an oscillation. Such experimentally recorded oscillations have sometimes been ascribed

to transducer or amplifier circuits; but Eq.(89) shows that the oscillations are in the bar itself.

The discontinuity in Fig.27 at $\tau_1 = 173.2$ corresponds to one characteristic velocity, $\sqrt{G/\rho}$. The disturbances before this time are allowed by the infinite characteristic velocity. It should be mentioned that Eqs.(86) and (87) permit the use of the Pochhammer results for sinusoidal waves, since $\omega(\kappa)$, $\frac{\partial \omega}{\partial \kappa}(\kappa)$, and $\frac{\partial^2 \omega}{\partial \kappa^2}(\kappa)$ can be computed exactly for the first radial mode. The discontinuity would then travel with the Rayleigh surface wave velocity.

The Lapace transform, where

$$\overline{U} = \int_0^\infty U e^{p\tau_1} d\tau_1 \tag{96}$$

was also investigated as a possible method of solving Eq.(50) by eliminating time as a variable, and solving the resulting differential equation in ξ. This gives the result that:

$$\overline{U} = const.\ e^{-\alpha \xi} \tag{97}$$

where α is determined by the fourth order algebraic equation:

$$\alpha^4 - \left(\frac{E}{G} p^2 + 1\right)\alpha^2 + p^2 = 0. \tag{98}$$

Approximate methods of inverting Eq. (96) seem extremely tedious. With regard to an exact inversion of $\overline{U}$, Miklowitz (30) has tried this on the Herrmann-Mindlin equation, Eq.(54), but the determination of numerical results has been hindered

by rapidly oscillating integrands of large amplitude.(31).

Influence of Boundary Conditions

To make the lateral surfaces of the bar stress-free, it is necessary that the axial displacement be a function of the radius as well as x and t. This may be achieved by taking:

$$u = (1 + \beta\frac{r^2}{a^2})u_o(x,t) \tag{99}$$

and setting σ_r equal to zero. This determines v since:

$$\sigma_r = \lambda(e_x + e_r + e_\theta) + 2\mu e_r \tag{100}$$

where λ and μ are Lame's constants. Thus:

$$0 = \lambda\left(\frac{\partial u}{\partial x} + \frac{\partial v}{\partial r} + \frac{v}{r}\right) + 2\mu\frac{\partial v}{\partial r}. \tag{101}$$

Now substituting from Eq.(99) into Eq.(101) gives:

$$\left(\frac{1-\nu}{\nu}\right)\frac{\partial v}{\partial r} + \frac{v}{r} = -\left(1 - \beta\frac{r^2}{a^2}\right)\frac{\partial u_o}{\partial x} \tag{102}$$

for which the solution is

$$v = A_1 r^{-\frac{\nu}{1+\nu}} - \nu\frac{\partial u_o}{\partial x}\left(r - \frac{\beta}{3-2\nu}\frac{r^3}{a^2}\right). \tag{103}$$

Since v = 0 at r = 0, $A_1 = 0$. To determine β, the shear strain at the surface of the bar is set equal to zero;

$$0 = \gamma_{xr}(a) = \frac{\partial u}{\partial r} + \frac{\partial v}{\partial x} = -2\frac{\beta u_o}{a} - \nu a\frac{\partial^2 u_o}{\partial x^2} + \frac{\nu\beta a}{3-2\nu}\frac{\partial^2 u_o}{\partial x^2}. \tag{104}$$

Hence β is determined by:

$$\beta = - \frac{\nu a^2 \partial^2 u_o / \partial x^2}{2 u_o - \frac{\nu a^2}{3-2\nu} \frac{\partial^2 u_o}{\partial x^2}} . \tag{105}$$

For sinusoidal stress waves given by Eq.(51), the value of β is:

$$\beta = \frac{4\nu\pi^2 a^2/\Lambda^2}{2 + \frac{4\nu\pi^2 a^2}{(3-2\nu)\Lambda^2}} . \tag{106}$$

By using Eqs.(99) and (103) for u and v, and substituting these into Eqs.(42), (44), (46), and (47), and using Hamilton's principle, Eq.(48), the phase velocity is found as:

$$c = c_o \sqrt{\frac{\Psi_1 + \frac{\nu^2\pi^2}{1+\nu}\left(\frac{a}{\Lambda}\right)^2 \Psi_2}{\xi_1 + 2\nu^2\pi^2\left(\frac{a}{\Lambda}\right)^2 \xi_2}} \tag{107}$$

where, for $\nu = 0.29$,

$$\left.\begin{aligned} \xi_1 &= 1 - \beta + \beta^2/3 \\ \xi_2 &= 1 - \frac{4\beta}{3(3-2\nu)} + \frac{\beta^2}{2(3-2\nu)^2} \\ \Psi_1 &= 1 - \beta + 0.3439\,\beta^2 \\ \Psi_2 &= \xi_2 - \frac{\beta}{\nu\pi^2}\left(\frac{\Lambda}{a}\right)^2\left(1 - \frac{2\beta}{3(3-2\nu)}\right) + \frac{\beta^2}{4\nu^2\pi^2}\left(\frac{\Lambda}{a}\right)^4 \end{aligned}\right\} \tag{108}$$

Equation (107) has the same form as Eq.(53), and it has been plotted as Curve V in Fig.26 , where it is seen that it fits the exact solution Curve I most closely. Figure 28 is a comparison of the axial displacement u, given by Eq.(99) to the exact solution as found by Davies (32) for $a/\Lambda = 0.196$. It thus appears that significant improvement in approximate analyses must be obtained by including additional longitudinal

modes so that the cross-section is free to warp. It is seen from Fig. 26 that $a/\Lambda = 0.8$ is the regime of surface waves and no approximation that assumes plane sections can give satisfactory results in this range.

Summary

The approximate methods of investigating stress propagation in a bar, because of the very nature of the approximations, cannot give quantitative results when relatively short period waves are involved. At best, the methods can be expected to give only qualitative information in this regard. The differential equation, Eq.(50), contains sufficient physical properties of the problem so that its solution for the case of a concentrated initial disturbance shows dispersive oscillations which is in qualitative agreement with experimental observations. Equation (50) is an improvement of the Rayleigh-Love theory in that it has one finite characteristic velocity, and because its sinusoidal wave speeds vary with wave length in a manner similar to the first made of the exact theory. But this differential equation, together with those of Love, and Mindlin and Herrmann suffers from two defects: the internal stresses described by it are not in agreement with those of the exact solution, and the boundary conditions are not satisfied in that the surface of the bar is not stress-free. An appreciable improvement is obtained at longer wave lengths by making the boundary stress-free, which indicates that a more accurate approximate theory must include higher longitudinal modes.

VI CONCLUSIONS

Several important criteria for the testing and evaluation of photoelastic plastics for dynamic photoelasticity can now be formulated. First, since the stress-fringe constant of several photoelastic plastics has been found to depend upon the rate of loading, it is necessary to make strain measurements in order to determine the strain-fringe constant. For CR-39, this measurement gives a dynamic value of the strain-fringe constant of 3.42×10^{-4} in/fringe $\pm$ 3%, which apparently is independent of the rate of loading. This value differs from the static strain-fringe constant by less than 2%, which is within the experimental error.

Second, most plastics are viscoelastic; that is, each of the Fourier components of a stress wave travels with its own speed and has its own damping factor. Thus, to determine the mechanical properties of a plastic it is necessary to make tests with sinusoidal stress waves and to find the elastic modulus, the wave speed, and the attenuation factor for each wave length. If the elastic modulus and the wave speed is constant, and if the damping is low, then correlation of the experiments to metals is possible. CR-39 was found to be a nonlinear viscoelastic plastic with frequency dependent wave speed, and large attenuation which also depends upon the frequency. Hence, correlation to metals of experiments using CR-39 can be made only if the rise time of the stress

wave is relatively long, say greater than 25 microseconds, and if the stress level is low. A complete study of available photoelastic materials is necessary so that the plastic with the most favorable mechanical properties can be selected.

Third, the analysis of waves in bars in Part V indicates that the Boussinesq theory is not satisfactory for the computation of stresses or elastic modulii from experiments in bars which have stress waves with rapid rise times, even if the material is elastic. The theory can be used only if the leading edge of the stress wave has a length that is many times greater than the thickness of the bar. Thus, previous computations by other investigators, which utilized the Boussinesq theory for elastic bars, may be in serious error since viscoelastic and dispersive effects are ignored in that theory. The analysis contained in Part V also indicates the extreme complexity of an analytic solution of impact in a bar.

As far as fringe recording devices are concerned, the Ellis ultra-high speed motion picture camera has proved satisfactory for obtaining photoelastic motion pictures at repetition rates up to 400,000 frames per second, and with an exposure time of 0.1 microsecond for each frame. The multiplier phototube has proven to be extremely sensitive to optical retardation, being capable of detecting a fraction of a fringe, and having a frequency response of at least 18 megacycles. It has the disadvantage, however, of being able to detect only those isochromatics passing by a small

area. Depending upon the problem being investigated, a combination of the two techniques may be necessary.

As a result of this investigation, the mathematical analysis of stress waves does not appear feasible for engineering purposes. The most satisfactory method of quantitatively analyzing stress waves is to use the equipment that was investigated and the techniques that were developed in this thesis.

APPENDIX

Correction of Strain Gage Measurements of Strain Waves, For the Error Caused by the Finite Length of the Strain Gage

Since the leading edge of a strain wave, such as shown in Fig. 17, has a length of about six times that of the length of the strain gage, a correction may be necessary to account for the finite length of the strain gage. This leading edge, as shown in Fig. 17(c), may be represented quite closely by:

$$\frac{\partial u}{\partial x} = A \sin^2 \frac{\pi}{2\tau} (x/c - t) \tag{108}$$

in which $\partial u/\partial x$ is the actual longitudinal strain e_1; A is the amplitude; τ is the rise time of the leading edge; and c is the speed of the wave along the bar. Equation (108) is plotted in Fig. 32 against experimental data for birefringence. The fit is extremely close, hence Eq. (108) represents the leading edge of the wave quite closely.

On the other hand, the strain gage output may be different because of its finite length, and can be represented as:

$$e_g = \frac{A}{2} - \frac{A'}{2} \cos \frac{\pi}{\tau} (t - \tau_{lag}) \tag{109}$$

where A' is the amplitude of the recorded strain, and T_{lag} is the time lag. The gage is centered at x = 0. Two different assumptions can be made concerning the strain gage, (1) that the strain gage measures the average strain over the

entire length a of the paper backing, and (2) that strain is transmitted to the strain gage only through the ends of the paper backing. The effects of shear lag and cement creep are not considered in the following analysis, nor is the speed of propagation of strain in the gage and backing.

In case (1) above, for a continuing $\sin^2$ wave, the strain gage output is:

$$e_g = \frac{\int_{-a/2}^{a/2} \frac{\partial u}{\partial x}(x,t)\, dx}{\int_{-a/2}^{a/2} dx} . \tag{110}$$

Equation (108) is substituted above to obtain:

$$e_g = \frac{A}{2} - \frac{A\tau c}{\pi a}\left[\sin\frac{\pi a}{2\tau c}\cos\frac{\pi t}{\tau}\right]. \tag{111}$$

Hence, although there is no phase lag,

$$\frac{A}{A'} = \frac{\pi a/2\tau c}{\sin \pi a/2\tau c} . \tag{112}$$

In terms of

$$y = a/2\tau c \tag{113}$$

the amplitude ratio becomes:

$$\frac{A}{A'} = \pi y / \sin \pi y . \tag{114}$$

As an example, if $\tau = 25 \times 10^{-6}$ sec, a = 0.5 in, and c = 6×10^4 in/sec, then y = 1/6, and A/A' = 1.048. Figure 29 is a plot of A/A' as given by Eq.(114) vs. y until the first infinity.

For case (2), which is the extreme from case (1), the recorded strain is given by:

$$e_g = \frac{u(a/2) - u(-a/2)}{a} \tag{115}$$

Using a trigonometric identity, Eq.(108) becomes:

$$\frac{\partial u}{\partial x} = \frac{A}{2}\left[1 - \cos\frac{\pi}{\tau}(x/c - t)\right]. \tag{116}$$

Hence by integration,

$$u = \frac{Ax}{2} - \frac{Ac\tau}{2\pi}\sin\frac{\pi}{\tau}(x/c - t), \tag{117}$$

By substitution in Eq.(115),

$$e_g = \frac{A}{2} - \frac{Ac\tau}{2a\pi}\left[\sin\frac{\pi}{\tau}(a/2c - t) + \sin\frac{\pi}{\tau}(a/2c + t)\right], \tag{118}$$

giving the same result as in case (1).

The preceding equations have been derived for a continuous wave, but the leading edge of the wave, given by Eq.(108) only applies when $0 < t - x/c < \tau + T_o$, where $\tau + T_o$ is the duration of the trigonometric form. Hence Eq.(111) only applies while some portion of the sinusoidal part of the leading edge covers the entire length of the strain gage, that is, $a/2c < t < \tau + T_o - a/2c$.

To obtain e_g between the time that the leading edge of the strain first encounters the strain gage paper backing, and the time when the entire backing has the trigonometric portion of the wave on it, the limits of integration must be changed to

-a/2 as lower limit to ct as upper limit, with $-a/2c < t < a/2c$; that is:

$$e_g = \left[\frac{Ax}{2a} + \frac{ATc}{2\pi a}\sin\frac{\pi}{T}(t - x/c)\right]_{-a/2}^{ct} \qquad \frac{-a}{2c} < t < \frac{a}{2c} \tag{119}$$

which, by using Eq. (113) integrates to:

$$e_g\left(\frac{t}{T}\right) = \frac{A}{2}\left[\frac{t/T}{2y} + \frac{1}{2} - \frac{1}{2\pi y}\left(\sin\frac{\pi t}{T}\cos\pi y + \sin\pi y\cos\frac{\pi t}{T}\right)\right],$$

$$-y < \frac{t}{T} < y \tag{120}$$

The complete solution is then Eqs. (111) and (120), rewritten below in dimensionless form:

$$\left.\begin{aligned} \frac{e_g(t/T)}{A} &= \frac{1}{2}\left[\frac{t/T}{2y} + \frac{1}{2} - \frac{1}{2\pi y}\left(\sin\frac{\pi t}{T}\cos\pi y + \sin\pi y\cos\frac{\pi t}{T}\right)\right], \\ &\qquad -y < t < y \\ \frac{e_g(t/T)}{A} &= \frac{1}{2}\left[1 - \frac{1}{\pi y}\left(\sin\pi y\cos\frac{\pi t}{T}\right)\right], \quad y < \frac{t}{T} < 1 + \frac{T_o}{T} - y \end{aligned}\right\} \tag{121}$$

Figure 30 is a plot of the strain gage output given by Eq. (121), in comparison to the instantaneous strain at the center of the strain gage as given by Eq. (108) with x equal to zero. This has been plotted for $y = 1/6$, which is the value for the series of experiments described in Part II. Two points may be observed: first that the maximum e_g is $0.9775\,(\partial u/\partial x)_{max}$, an error of 2.25%; and secondly, the strain gage produces a signal before $t = 0$. This latter effect has been observed; for Fig. 17, shows that the rise time of the strain is slightly longer than the rise time of the birefringence. Since $y \simeq 1/6$

in this experiment, a correction of the data is made.

Concerning the assumptions, the qualitative effect upon the analysis of the previously omitted effects are as follows:

(a) Creep in the cement. Since the rise time of the stress wave is about $25\,\mu$sec, the effect of creep is probably negligible.

(b) Shear lag. This refers to the finite thickness of the wire strain gage, which causes the strain of the wire to be less than the strain in the specimen. This will increase the error.

(c) Finite velocity of propagation of wave in the strain gage. In the above analysis this velocity was assumed to be infinite, but it can be seen that the more nearly the properties of the gage backing matches the properties of the bar, the less will be the error.

It is not probable that the effect of (b) exactly cancels that of (c), but since the increased rise time for the leading edge has been observed; in the absence of more detailed information, corrections as computed from Eq. (121) are applied to the data of the dynamic experiments of Part II.

These correction factors are shown in Fig. 31 for $y = 1/6$. They are used to multiply the observed strain in order to obtain the actual strain. Figure 33 is a comparison of the actual recorded strain of run no. 8 with the theoretical strain given by Eq. (121).

REFERENCES

1. D. J. Coolidge, Jr. "An investigation of the mechanical and stress-optic properties of Columbia resin, CR-39," S.E.S.A. Vol. VI, No. 1. pp. 74-82.

2. A. Goetz. "A modified optical arrangement for photoelastic measurements," Rev. Sci. Instr., Vol. 5, No. 2, (1934) p. 84.

3. E. G. Coker and L. Filon, "Treatise on Photoelasticity," Cambridge Univ. Press, London, 1931. p. 200.

4. E. A. Ripperger, "Longitudinal impact of cylindrical bars," S.E.S.A. Vol. 10, No. 1. pp. 209-226.

5. H. Kolsky, "Stress Waves in Solids," Oxford, 1953.

6. R. W. Morse, "Dispersion of compressional waves in isotropic rods of rectangular cross-section," J. Acous. Soc. Am., Vol. 20, (1948). pp. 833-838.

7. D. Bancroft, "The velocity of longitudinal waves in cylindrical bars," Phys. Rev., Vol. 59, 1941. pp. 588-593.

8. D. A. Senior and A. A. Wells, "A photoelastic study of stress waves," Phil. Mag., Vol 7, (1946). pp. 463-469.

9. P. D. Flynn, "Studies in Dynamic Photoelasticity," PhD thesis, Ill. Inst. Tech., 1954.

10. B. Fried and N. H. Shoup, "A study in photoplasticity," TR No. 3, ONR Contract N7ONR-330-III Nr 064-121, State College of Washington, May 1953.

11. M. M. Frocht, "Kinematography in photoelasticity," Trans. A.S.M.E., Vol 54, (1932). pp. 83-96.

12. Z. Tuzi and M. Nisida, "Photoelastic study of stresses due to impact," Phil. Mag., Vol. 21, (1936). pp. 448-73.

13. W. M. Murray, "A photoelastic study in vibration," J.A.P. Vol. 12, (1941). pp. 617-22.

14. H. Schardin and W. Struth, Glastechn. Ber. Vol. 16, (1938). p. 219.

15. D. G. Christie, "An investigation of cracks and stress waves in glass and plastics by high-speed photography," Trans. Soc. Glass Tech., Vol 36, (1952). pp. 74-89.

16. H. C. Perkins, "Movies of stress waves in photoelastic rubber," J.A.M. Mar 1953, p. 140. (Trans. A.S.M.E. Vol. 75)

17. A. T. Ellis, "Observations on Cavitation Bubble Collapse," PhD thesis, Cal. Inst. Tech., Pasadena, 1952.

18. A. T. Ellis, "Production of accelerated cavitation damage by an acoustic field in a cylindrical cavity," Hydro. Lab. Report No. 21-14, Cal. Inst. Tech., Pasadena.

19. A. T. Ellis and M. S. Plesset, "On the mechanism of cavitation damage," Paper No. 54-A-76, ASME Annual Meeting, Nov. 1954, New York, N.Y.

20. H. Kolsky, op. cit., pp. 54-65.

21. R. W. Morse, "The velocity of longitudinal waves in rods of rectangular cross section," J. Acous. Soc. Am.,(1950), Vol. 20, p. 219.

22. Lord Rayleigh, "Theory of Sound," Vol I, Dover, p. 252.

23. A. E. H. Love, "The Mathematical Theory of Elasticity," 4th Ed., Cambridge, 1927, p. 428.

24. R. W. Morse, op. cit., 1948.

25. R. D. Mindlin and G. Herrmann, "A one-dimensional theory of compressional waves in an elastic rod," Proc. 1st U.S. National Congress of App. Mech., June 1951, Ann Arbor, Mich. pp. 187-191.

26. H. Kolsky, op. cit., p. 22

27. A. Sommerfeld, "Partial Differential Equations in Physics," Vol. 6, Academic Press, N.Y., 1950.

28. Sir H. Lamb, "Hydrodynamics," 6th Ed., Dover, N.Y., 1945. p. 395.

29. S. Petersson, "Investigation of stress waves in cylindrical steel bars by means of wire strain gauges," Trans. Roy. Inst. Technol., Stockholm, No. 62, 1953.

30. J. Miklowitz, "Travelling compressional waves in an elastic rod according to the more exact one-dimensional theory," 2nd U.S. Nat. Cong. App. Mech., Ann Arbor, Mich, June 1954.

31. J. Miklowitz, personal communication.

32. R. M. Davies, "A critical study of the Hopkinson pressure bar," Trans. Roy. Soc. London, Ser. A, No. 821, (1948), Vol. 240, p. 375.

33. M. M. Frocht, "Photoelasticity," Wiley, N.Y., 1948, Vol. II, pp. 333-428.

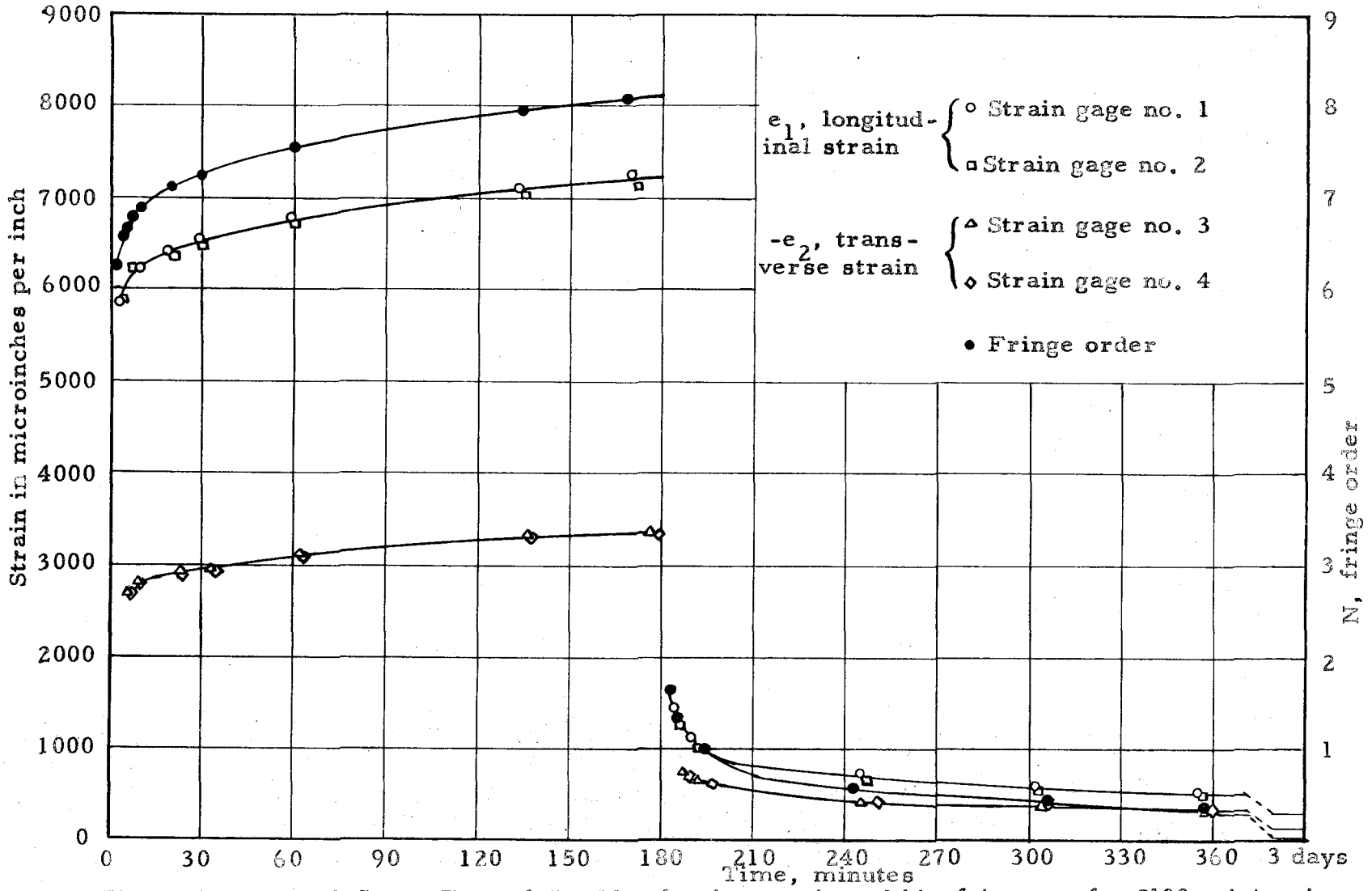

Figure 1. Typical Creep Test of CR-39, showing strain and birefringence for 2100 psi tension, specimen 0.252 inches thick.

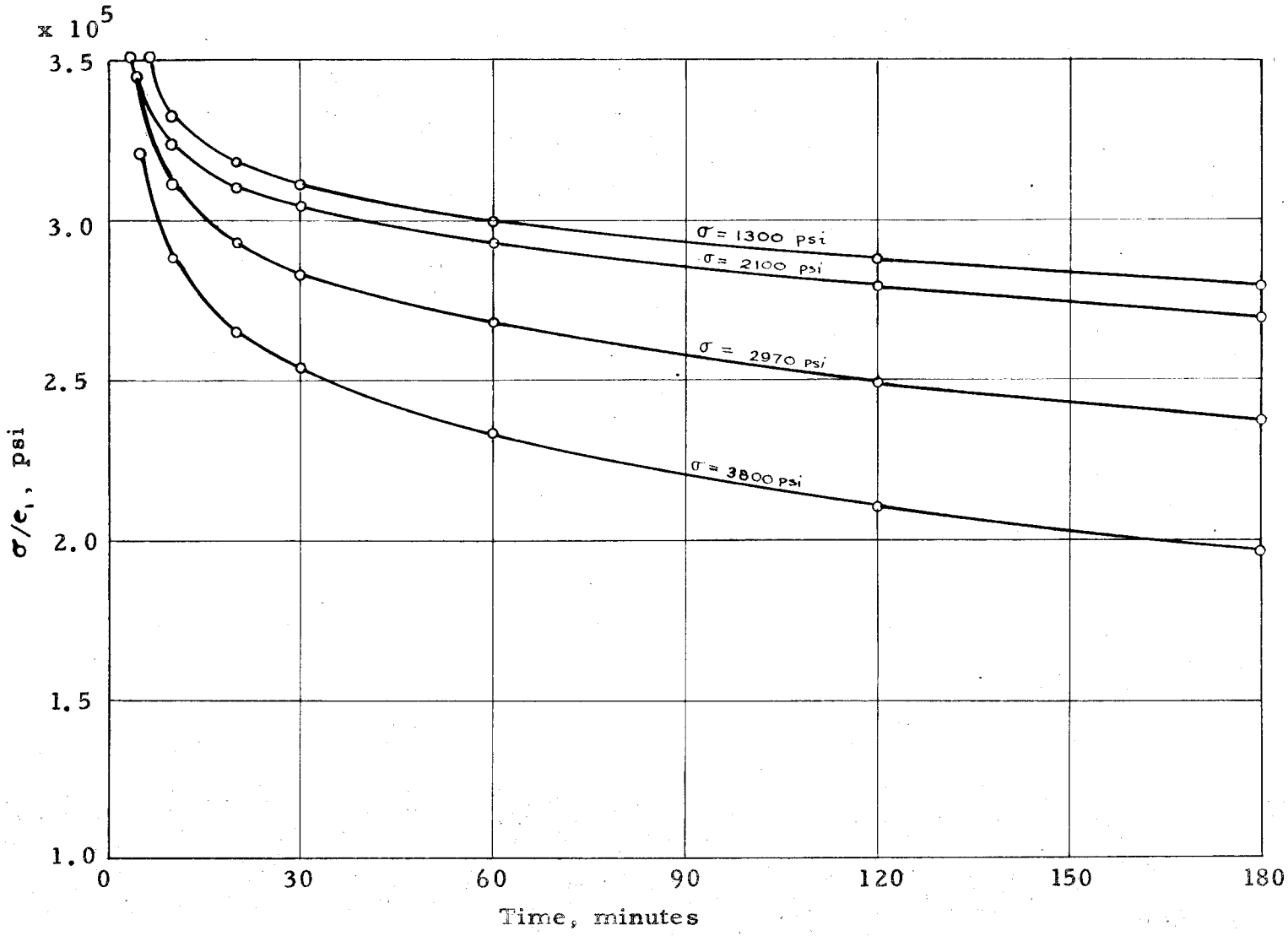

Figure 2. Ratio of stress to strain during creep tests of CR-39 tension specimen.

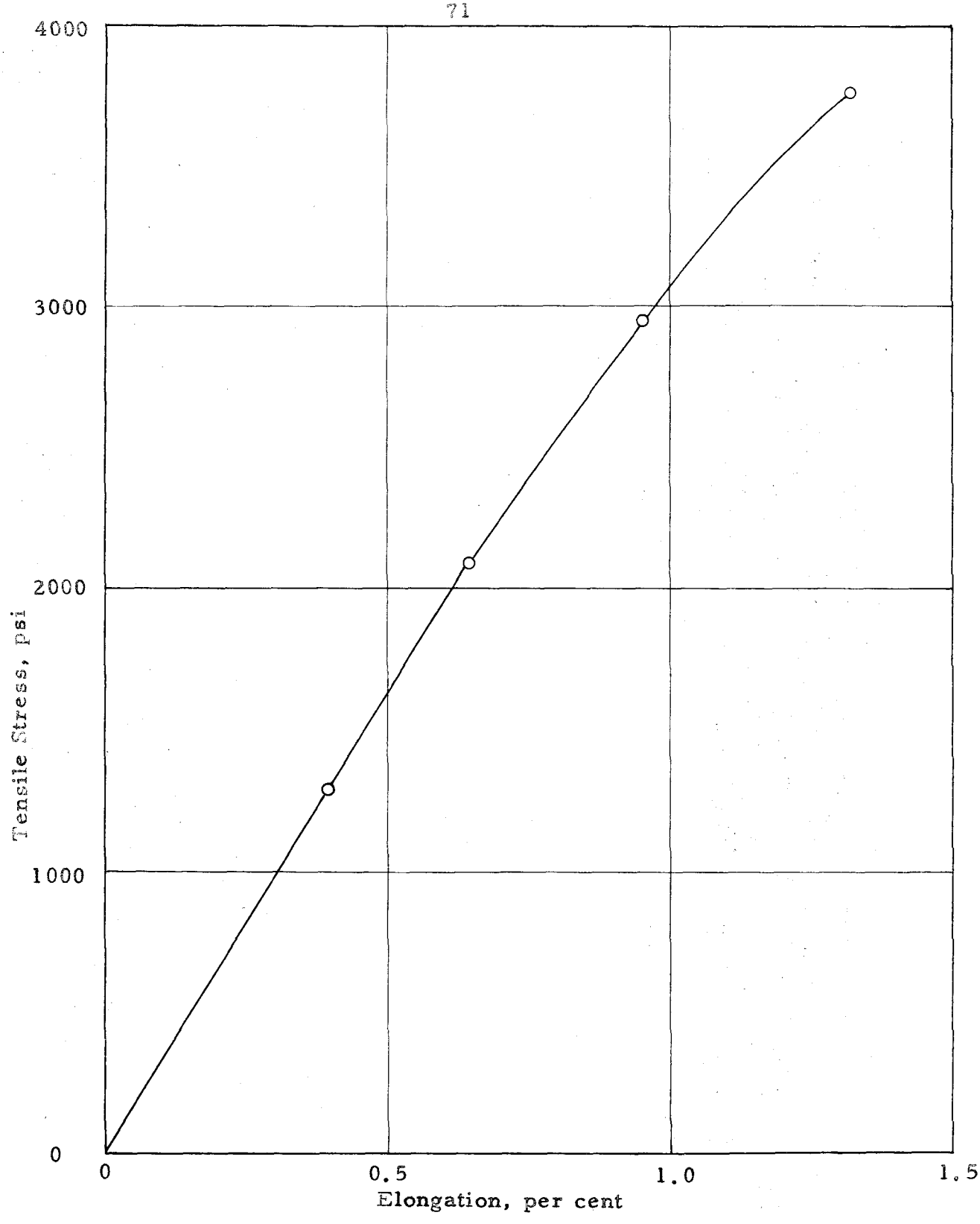

Figure 3. Tensile stress vs. longitudinal strain after 10 minutes of creep for CR-39 tensile specimen.

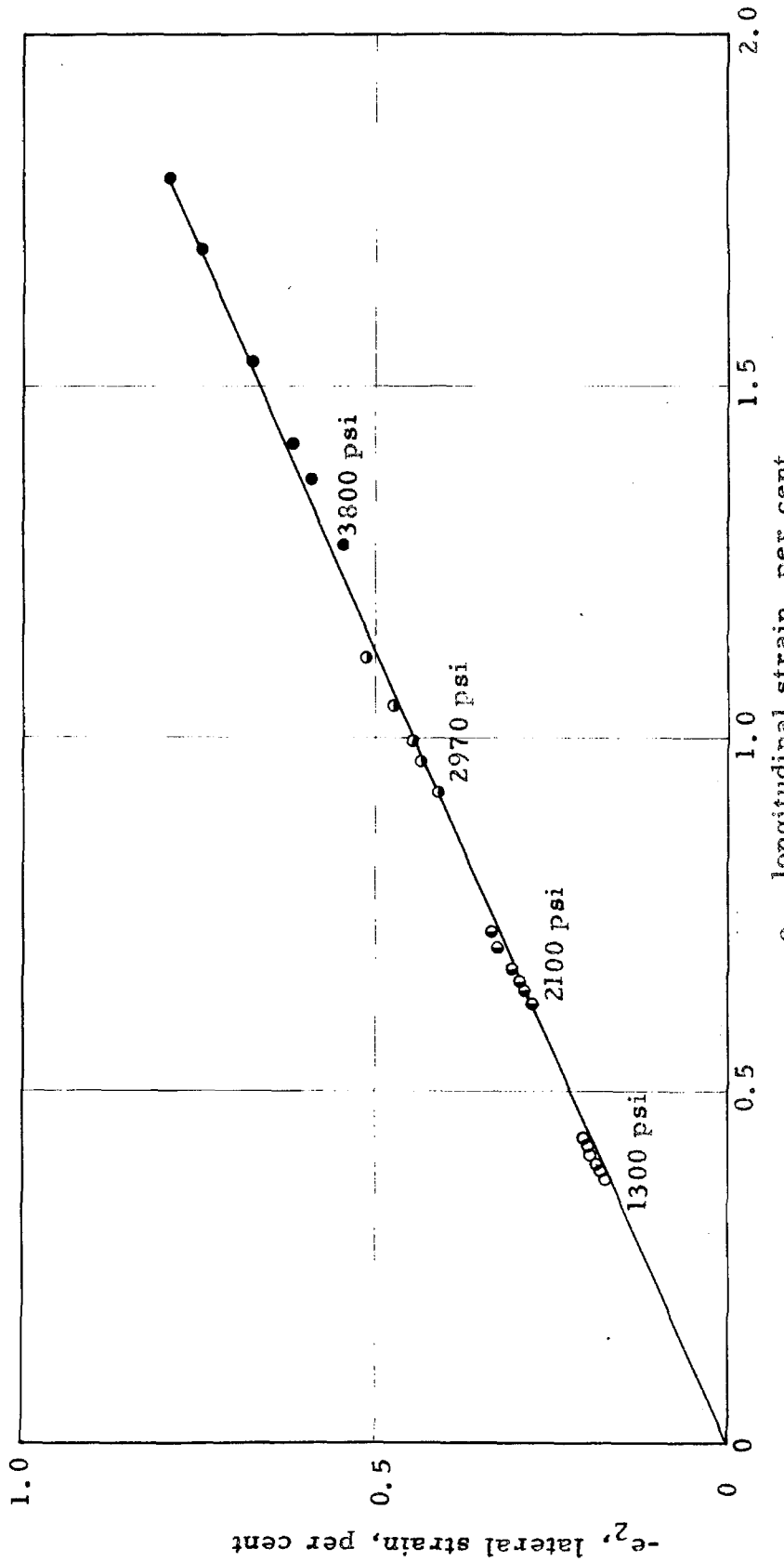

Figure 4. Lateral vs. longitudinal strain during creep tests of CR-39

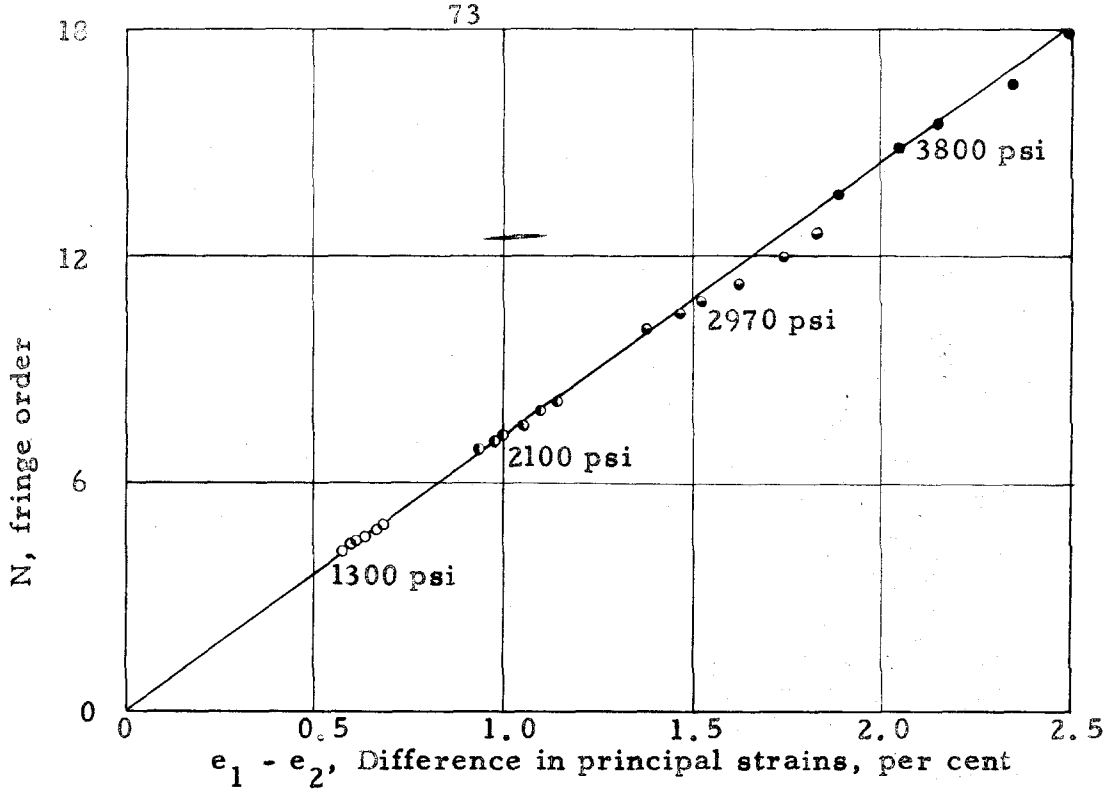

Figure 5. Birefringence vs. strain during creep for CR-39

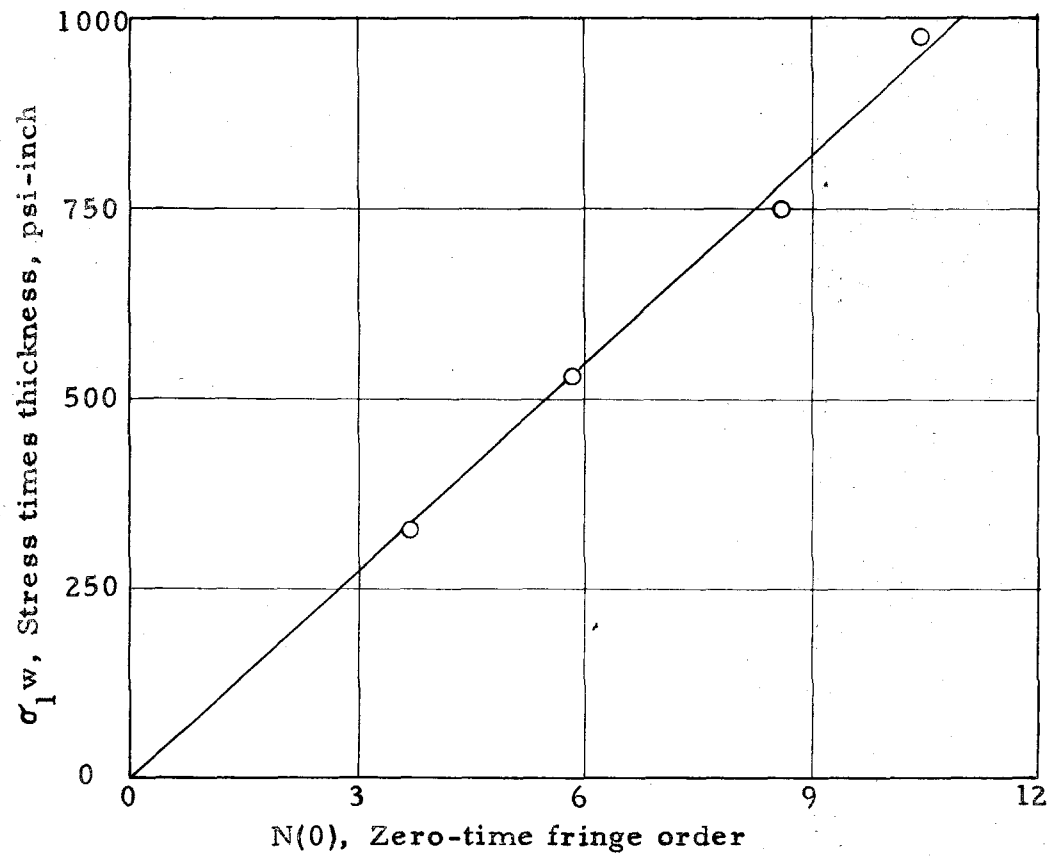

Figure 6. Zero-time fringe order vs. Stress for CR-39

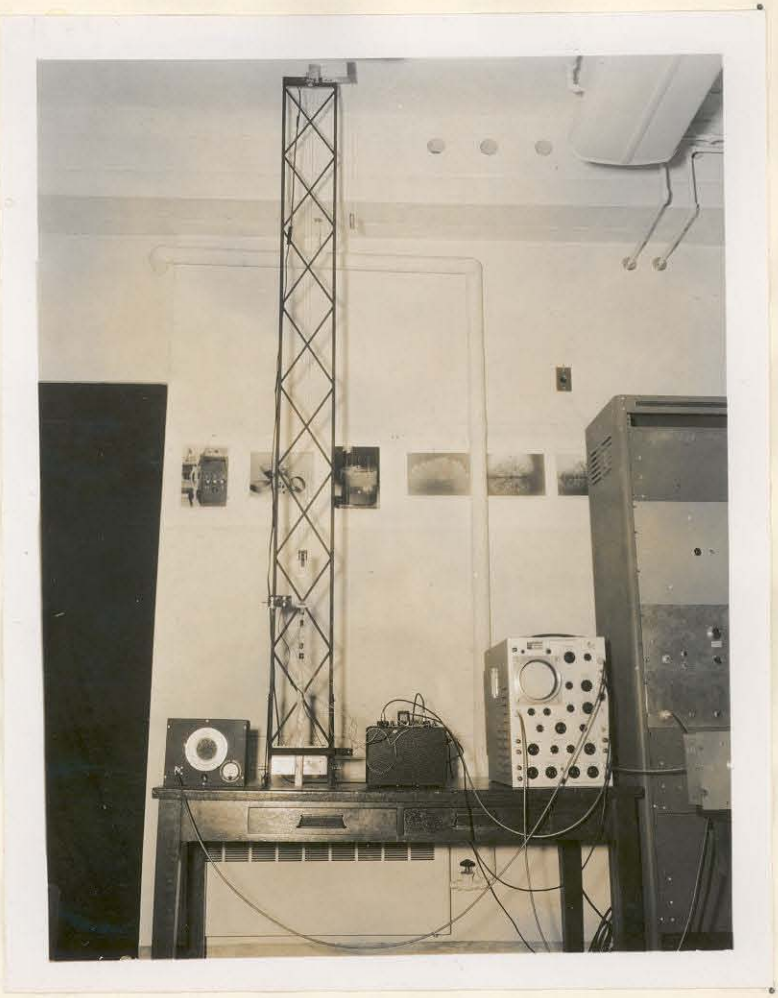

Figure 7. Dynamic loading apparatus. Left: photomultiplier. Center: loading frame with wire strain gages cemented to the specimen. Right: strain gage bridge and oscilloscope.

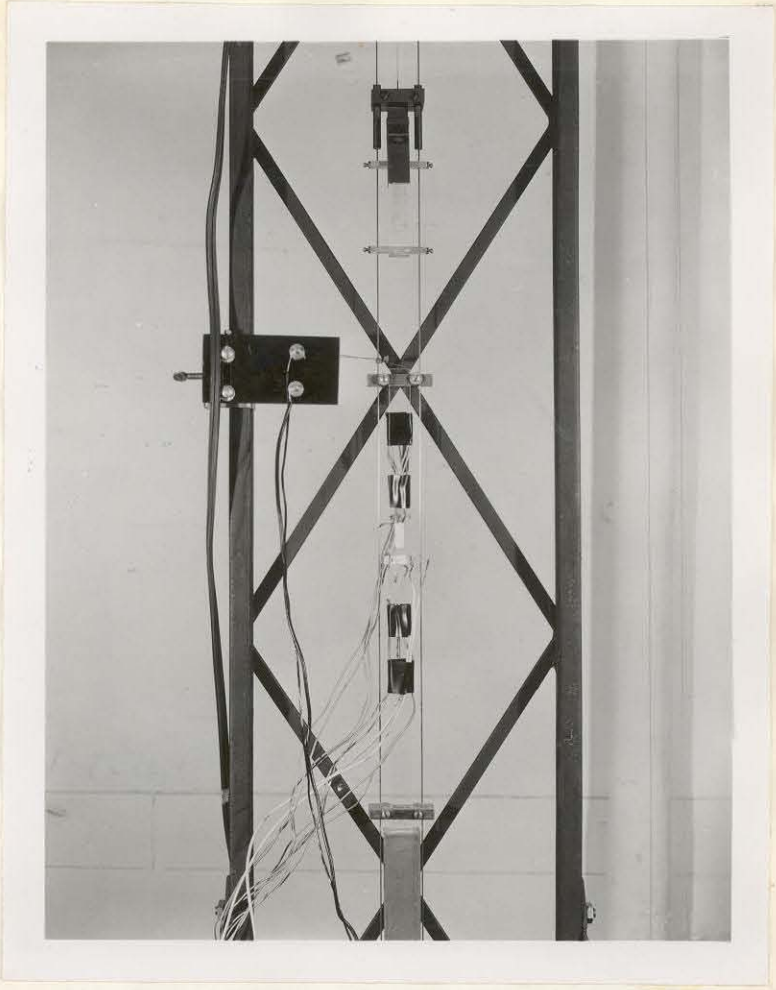

Figure 8. Close-up of dynamic loading apparatus.

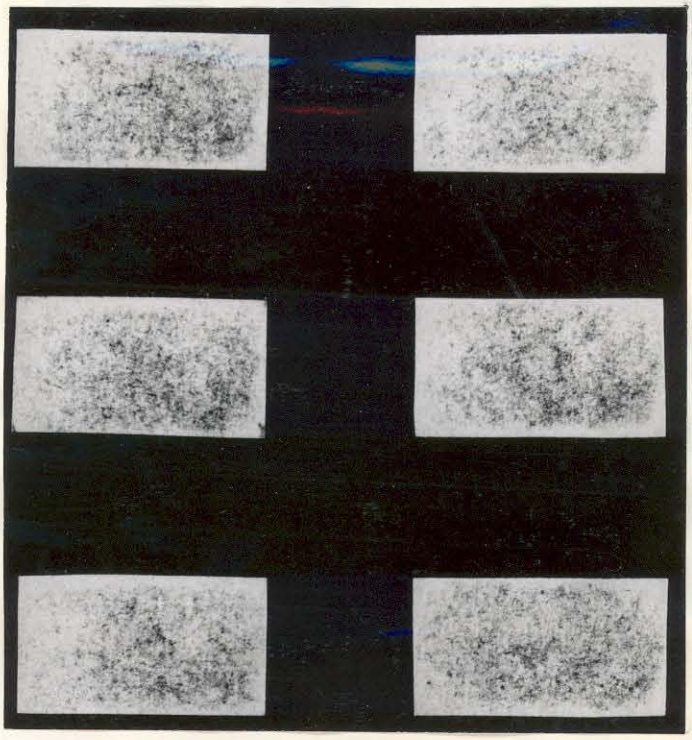

Figure 9. Carbon paper records of contact pressure during impact of hammer with specimen.

(a)

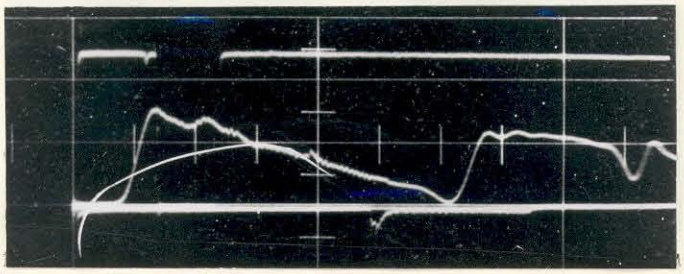

(b)

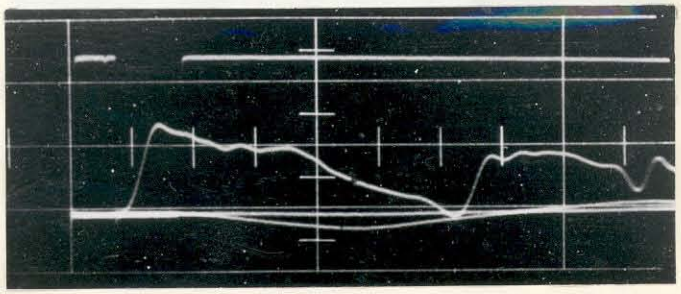

(c)

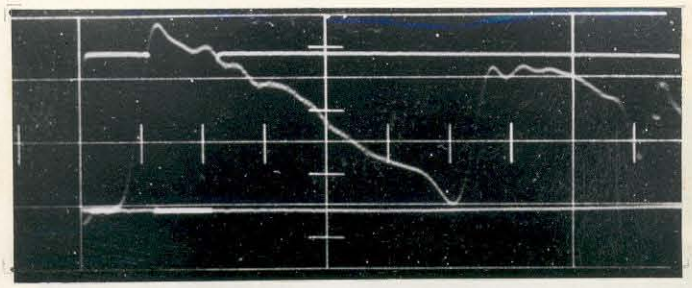

Figure 10. Longitudinal strain gage oscillograph records during impact. (a) Gage on front of specimen. (b) Gage on back of specimen. (c) Both gages additive.

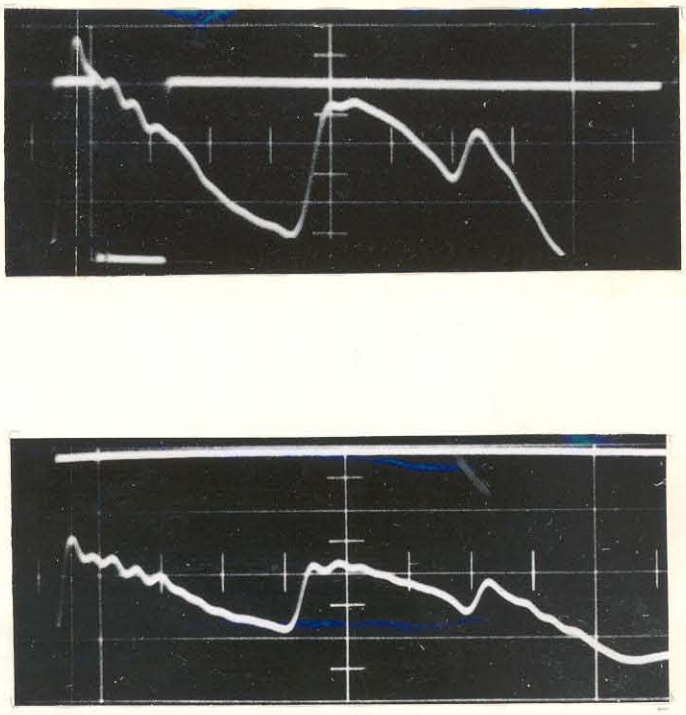

Figure 11. Oscillograph records of strain vs. time. Top: longitudinal strain. Bottom: transverse strain.

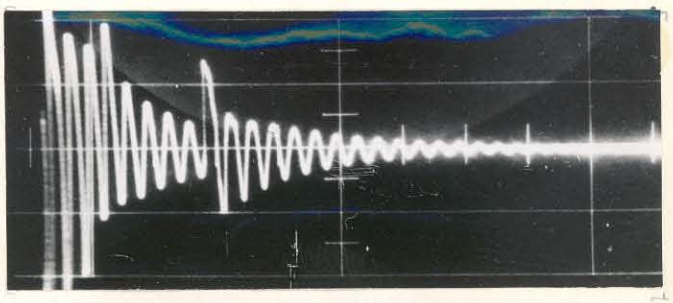

Figure 12. Strain gage oscillograph for free-free longitudinal vibrations of a bar of CR-39, excited by impact.

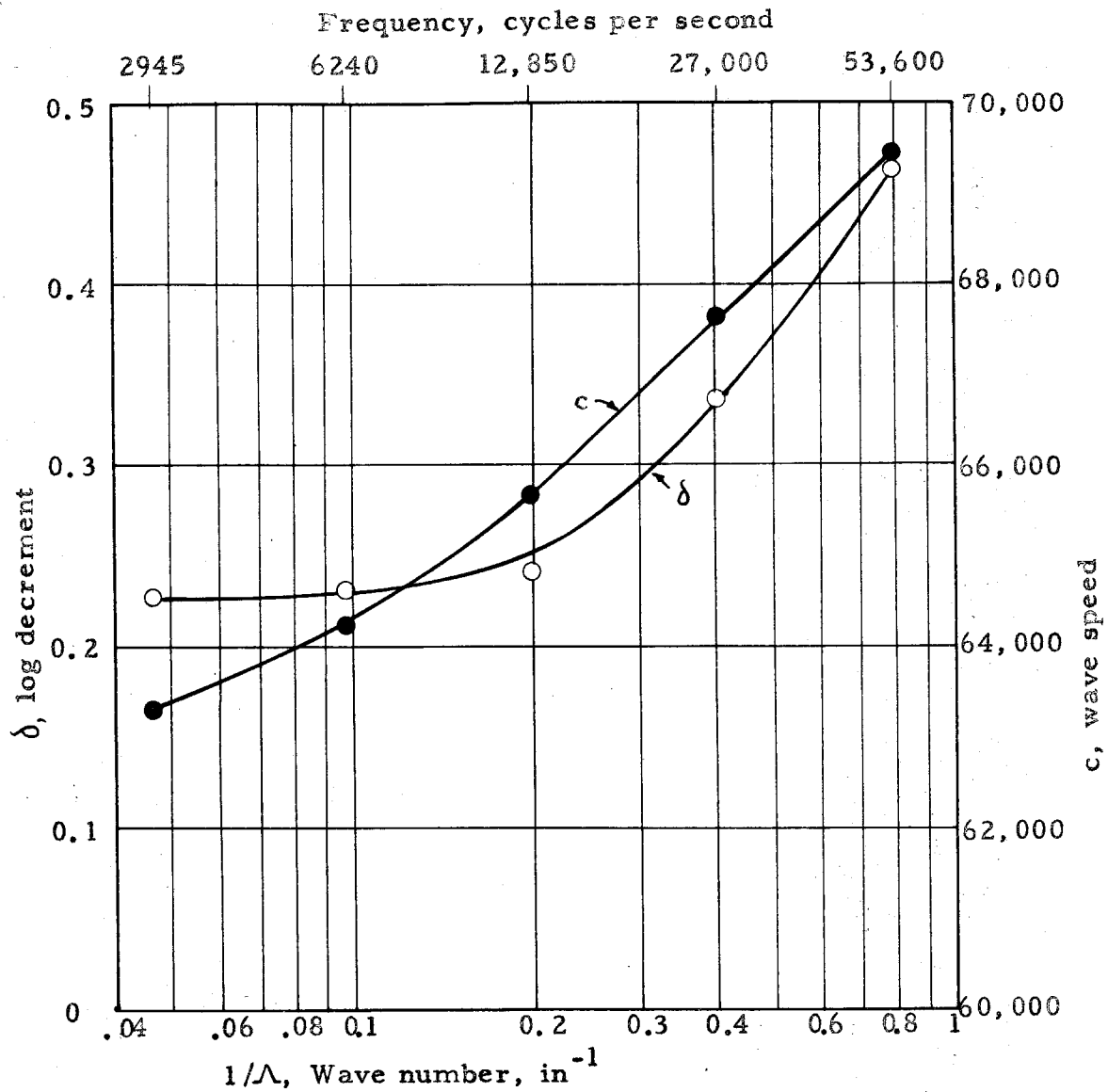

Figure 13. Wave speed and logarithmic decrement vs. frequency and wave number for CR-39.

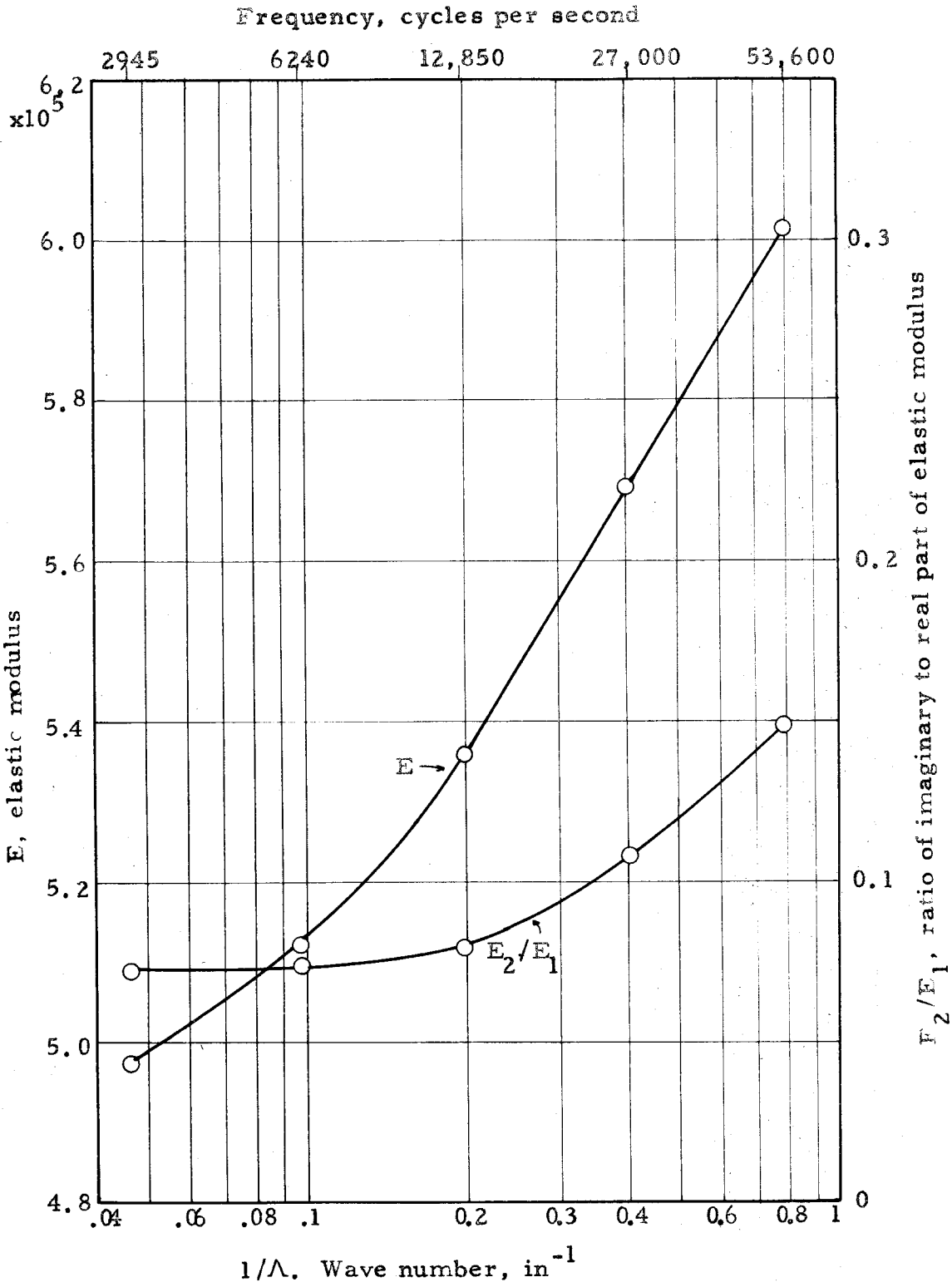

Figure 14. Elastic modulus and ratio of real to imaginary parts of elastic modulus vs. frequency and wave number for CR-39.

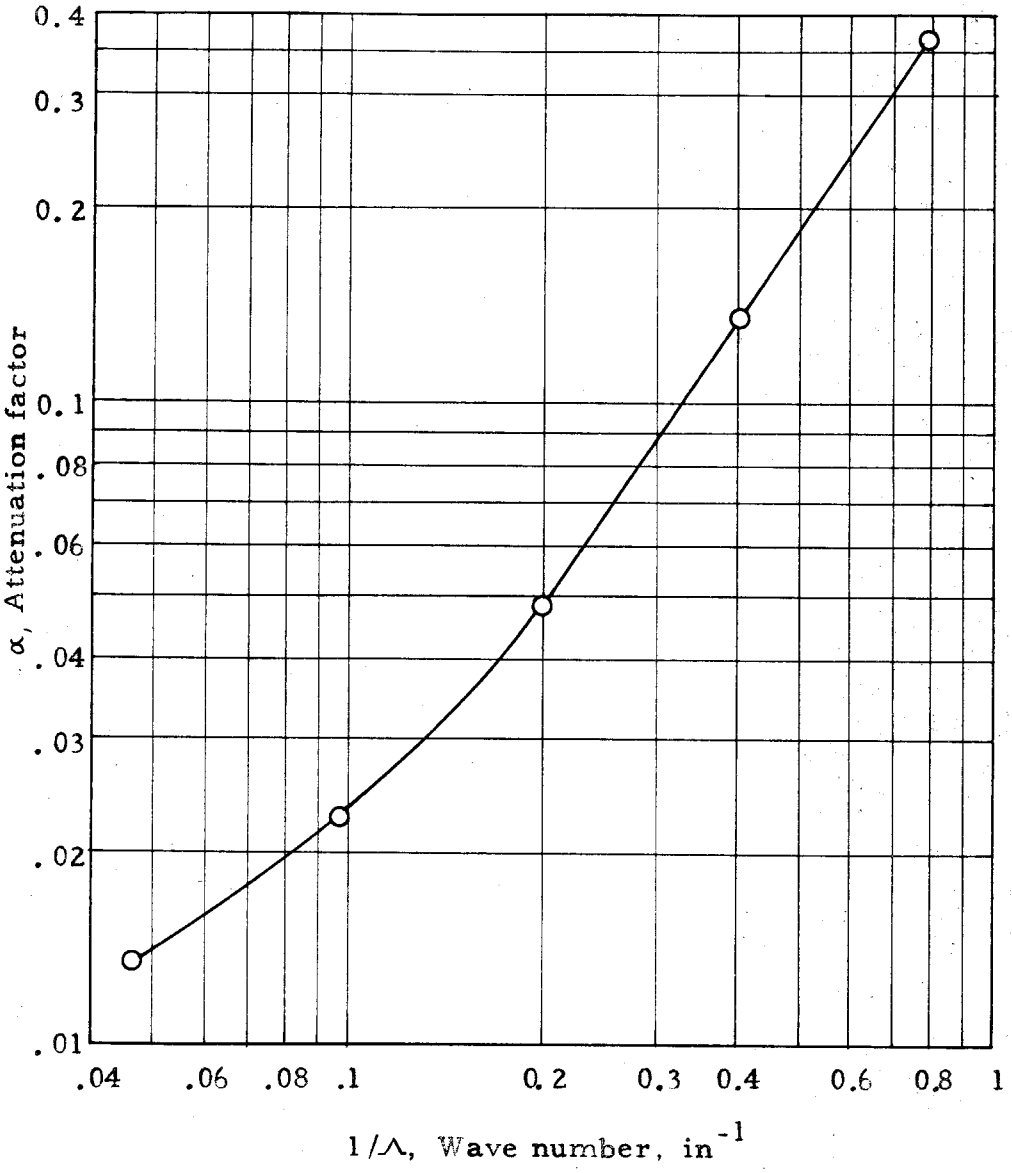

Figure 15. Attenuation factor α vs. wave number

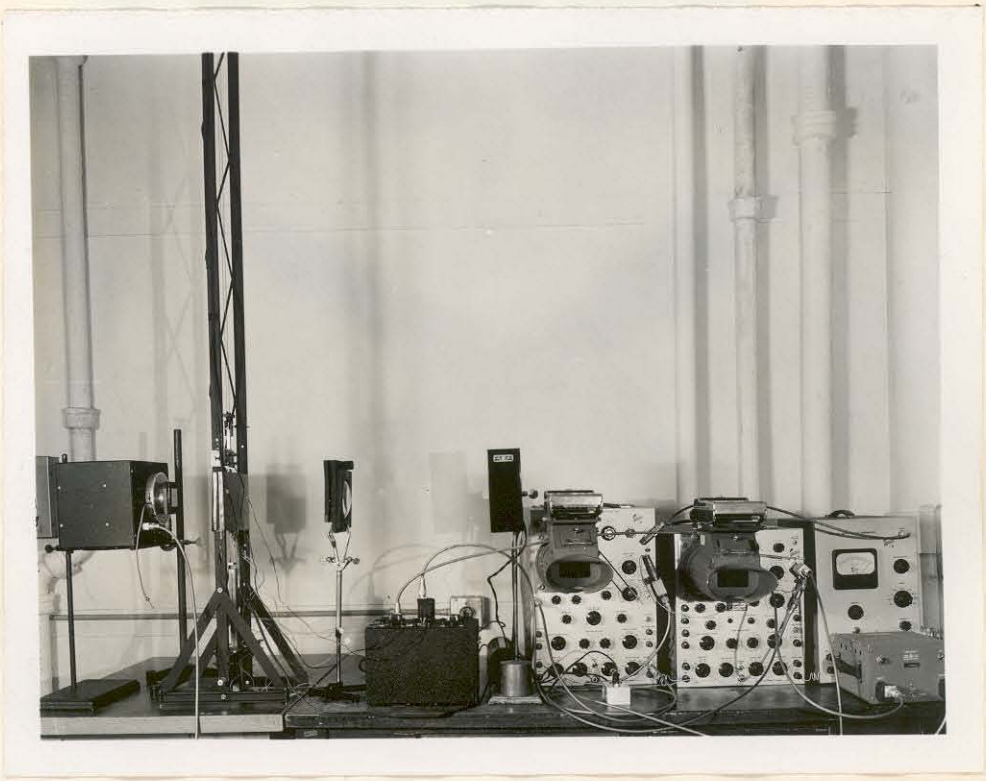

Figure 16. Apparatus for determining the dynamic strain-fringe constant. From left to right: multiplier photocell with filter, analyzer, and quarter-wave plate; loading frame; quarter-wave plate, polarizer and condensing lens; strain gage bridge; Hg lamp; two oscilloscopes; square wave generator; amplifier.

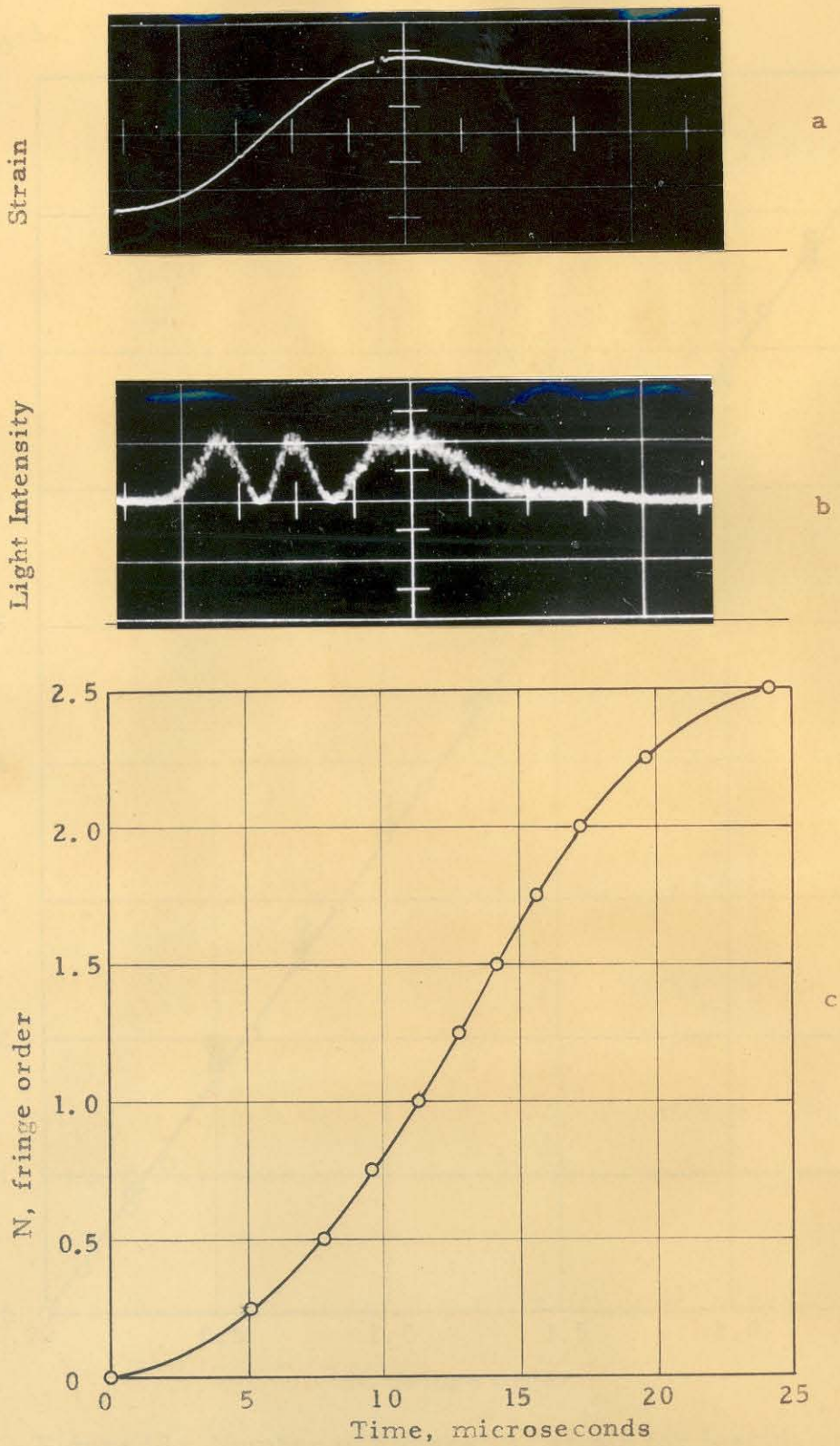

Figure 17. (a) Oscillograph record of longitudinal strain on leading edge of stress wave. (b) Oscillograph record of transmitted light. (c) Fringe order vs. time, from (b).

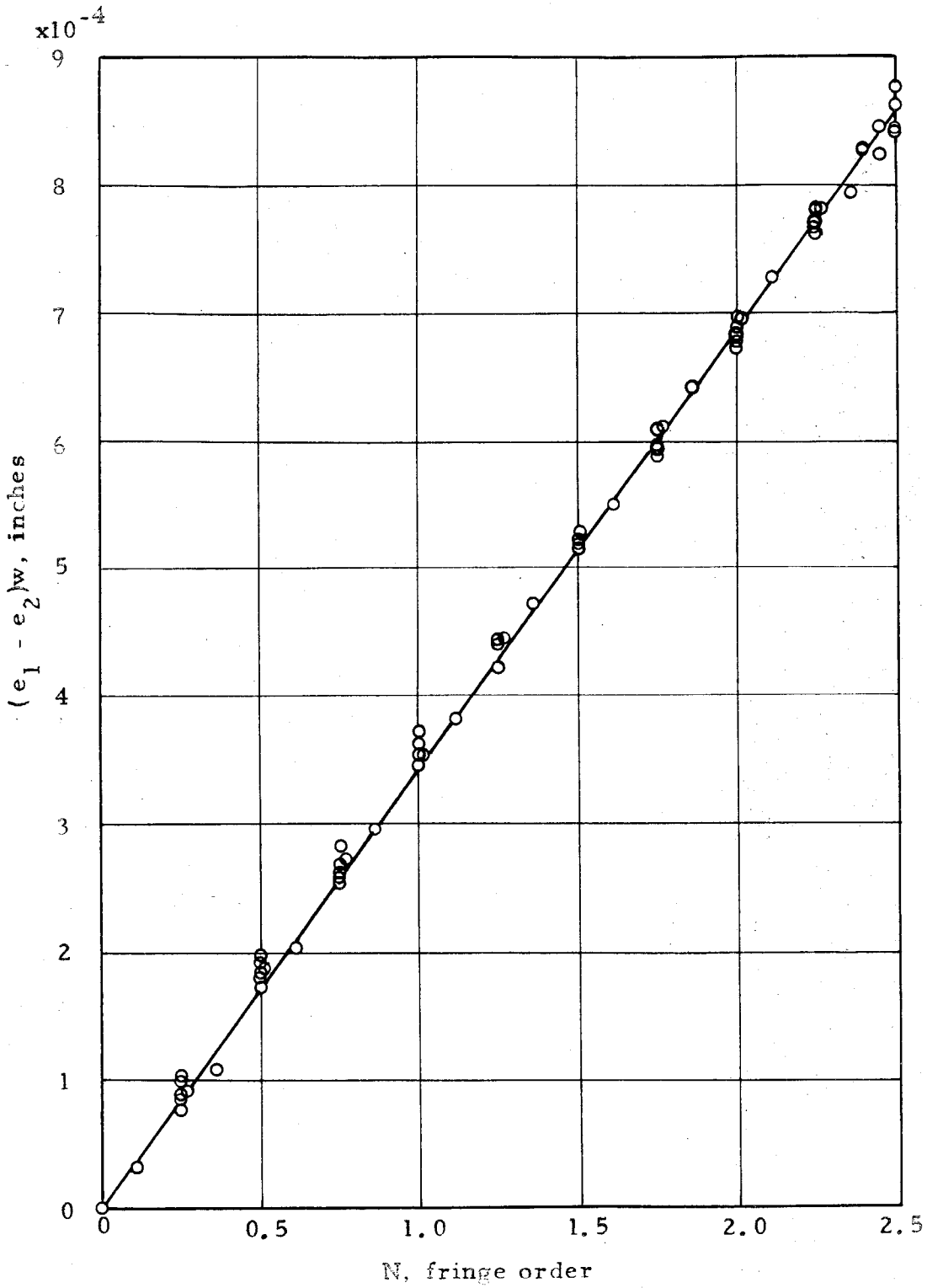

Figure 18. Number of fringes vs. strain for leading edge of stress wave for CR-39. Eight runs. 5461 Å

Figure 19. Ultra-high speed motion picture apparatus. Left foreground: cage containing flash tube capacitors. Center: timing and pulsing apparatus. Rear: camera and flash tube.

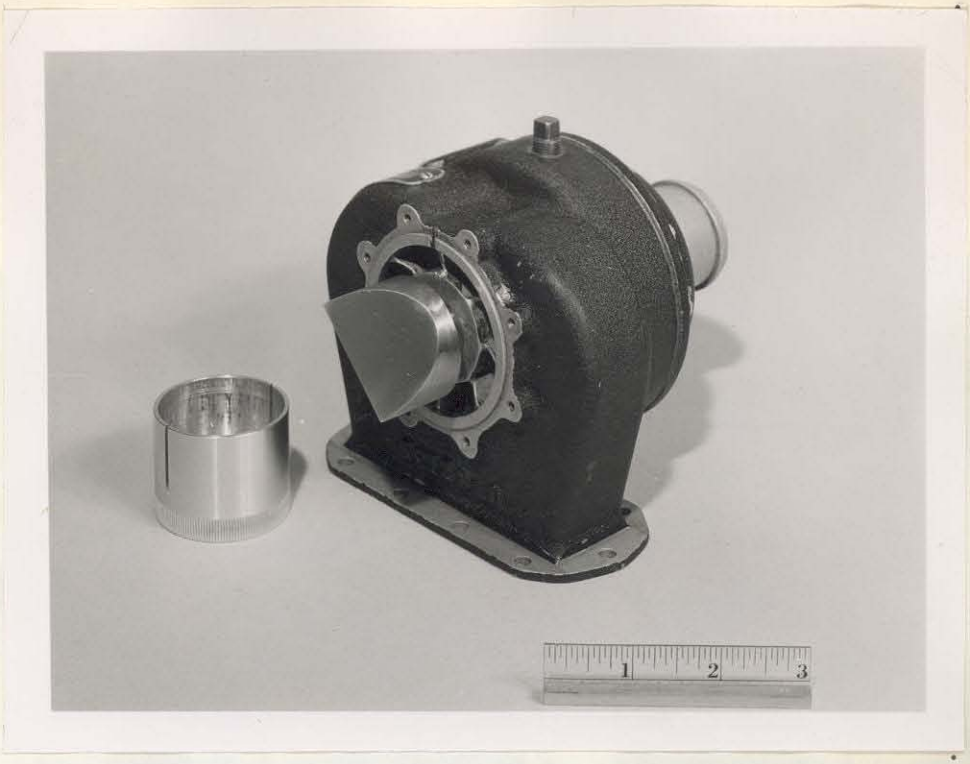

Figure 20. Rotating mirror and air turbine.

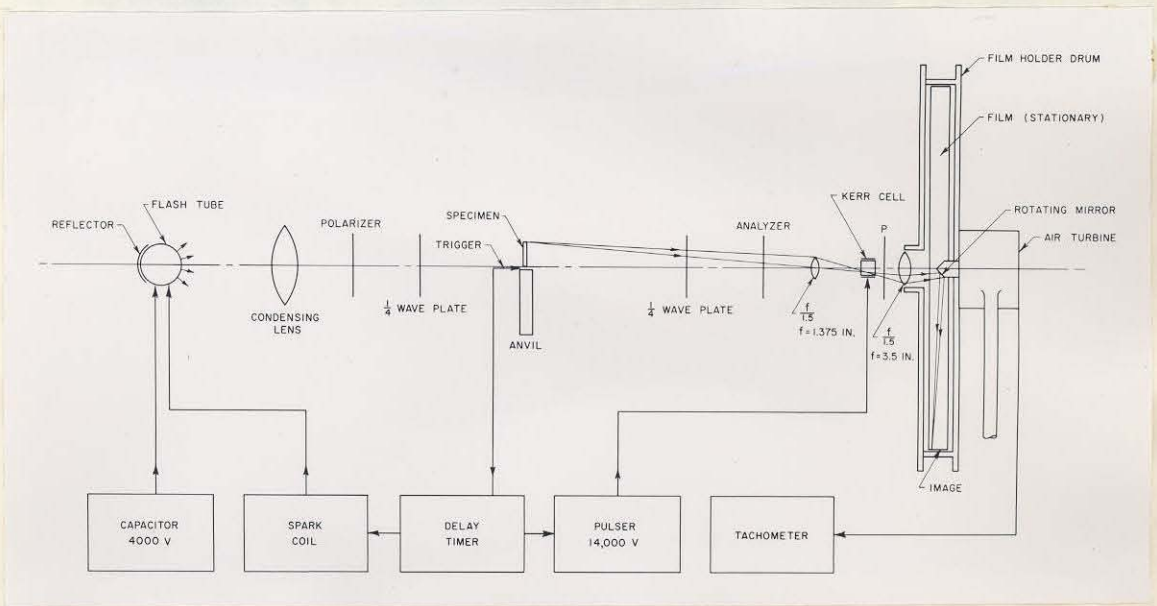

Figure 21. Schematic diagram showing arrangement for photographing transient waves with the ultra-high speed camera. Specimen strikes anvil.

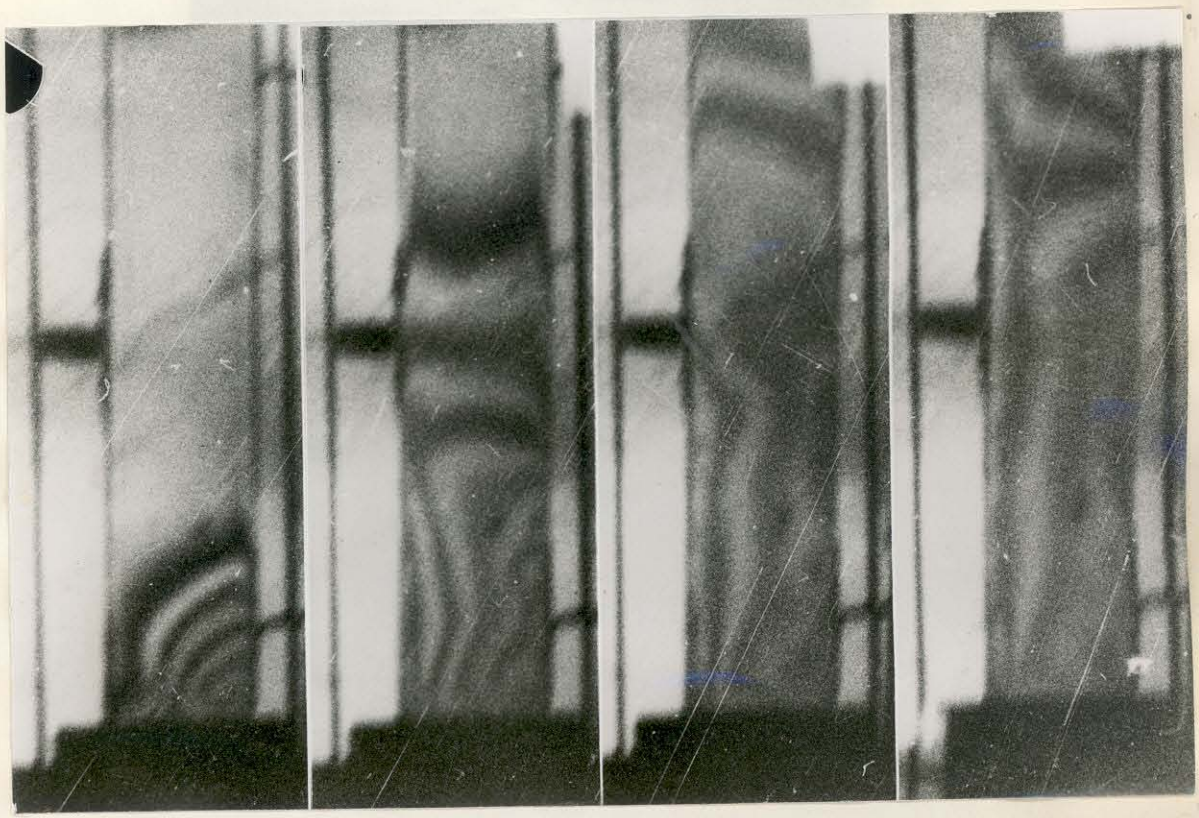

Figure 22. Four successive frames from ultra-high speed photoelastic motion pictures of stress waves in a bar of CR-39 striking a steel anvil. Exposure time of 0.1 microseconds. Time between frames, 20 microseconds.

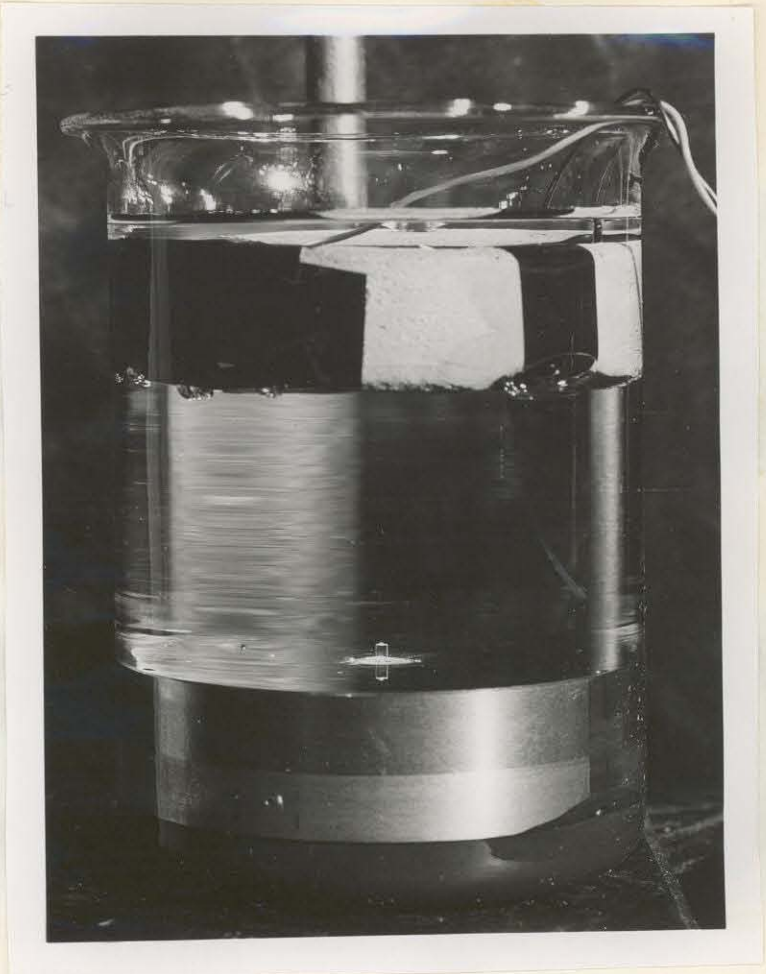

Figure 23. Acoustic cavitation in water. A small bubble cloud can be seen on top of the photoelastic specimen.

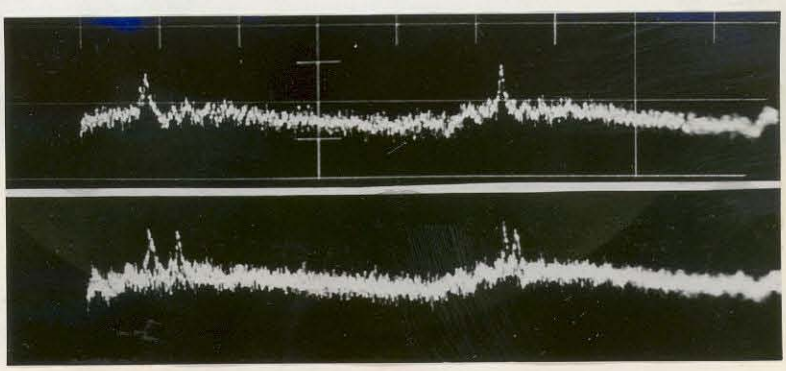

Figure 24. Oscillographs of the light intensity through a 0.004 x 0.004 in. slit centered 0.006 in. below the surface of a 1/16 x 1/16 x 1/8 in. CR-39 specimen when cavitation is occurring. Horizontal sweep time: 10 microseconds per division.

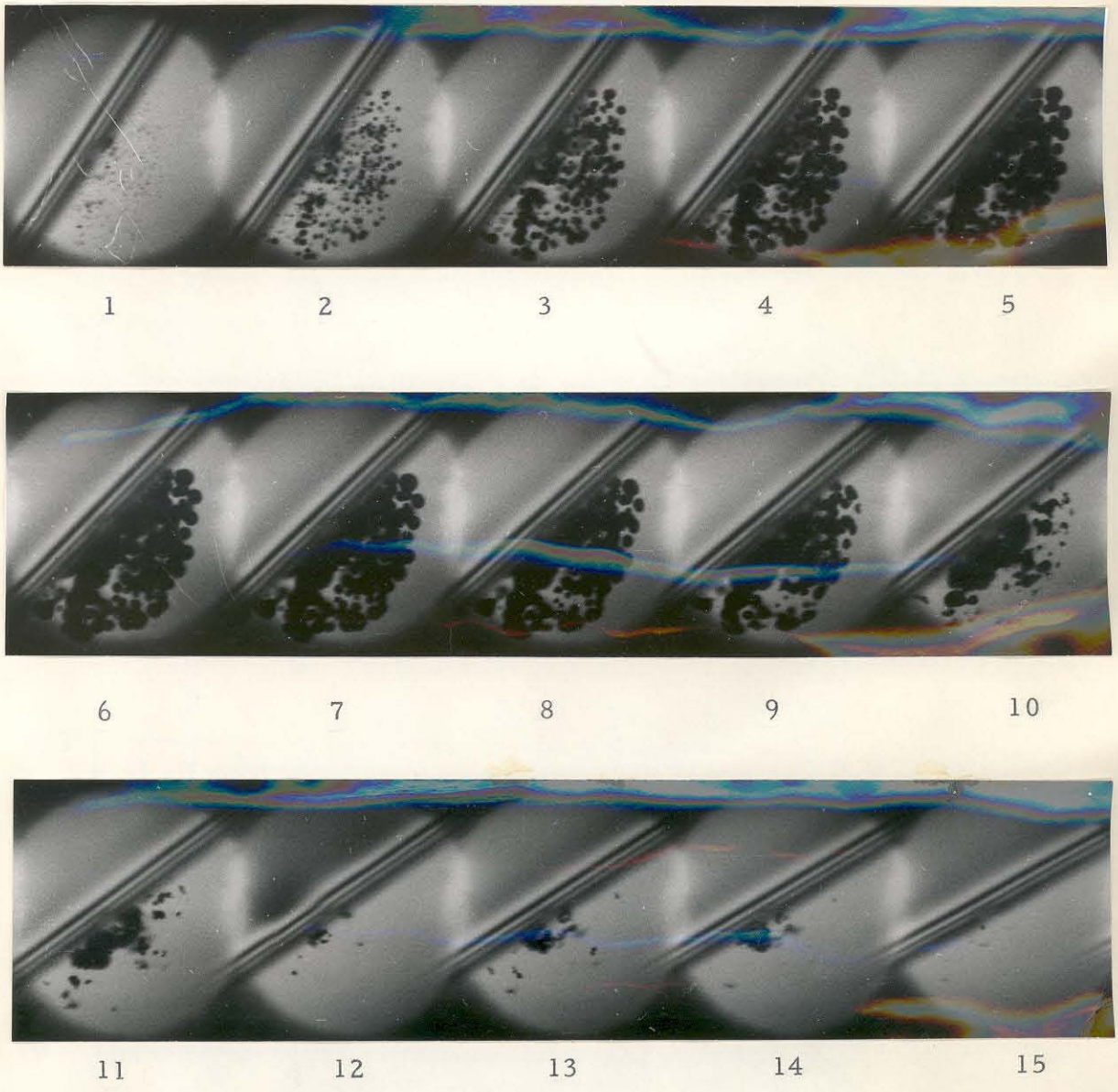

Figure 25. 10 kc. bubble cloud cycle, taken with ultra-high speed camera. Magnification: 10 X.

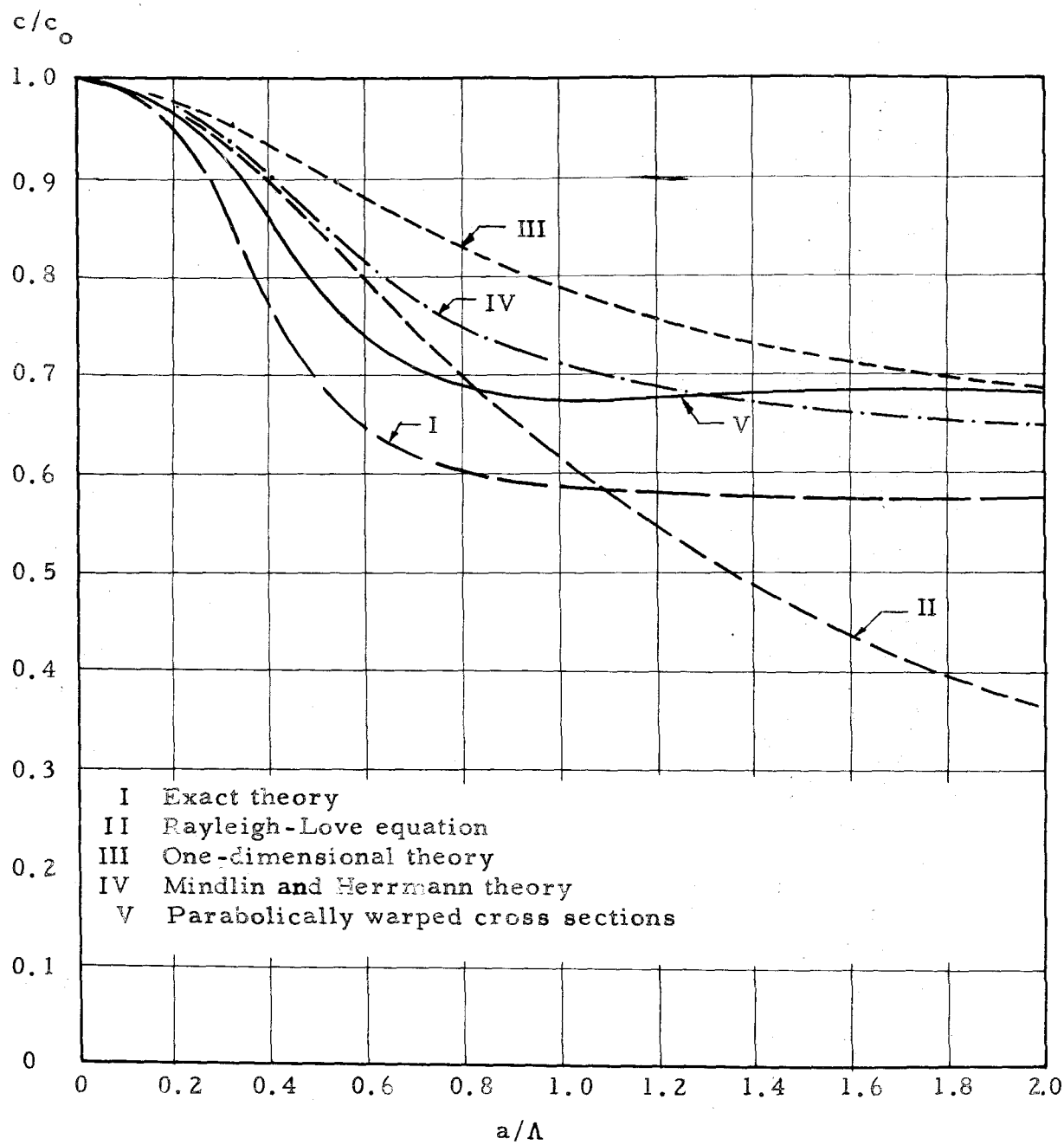

Figure 26. Phase velocity of sinusoidal stress waves according to various theories.

U
0
5
10
15
20
25
30
35
40
45
50
55
60
65
70
75
80
85
90
95
100
105
110
115
120
125
130
135
140
145
150
155
160
165
170
175
180
185
190
195
200
T

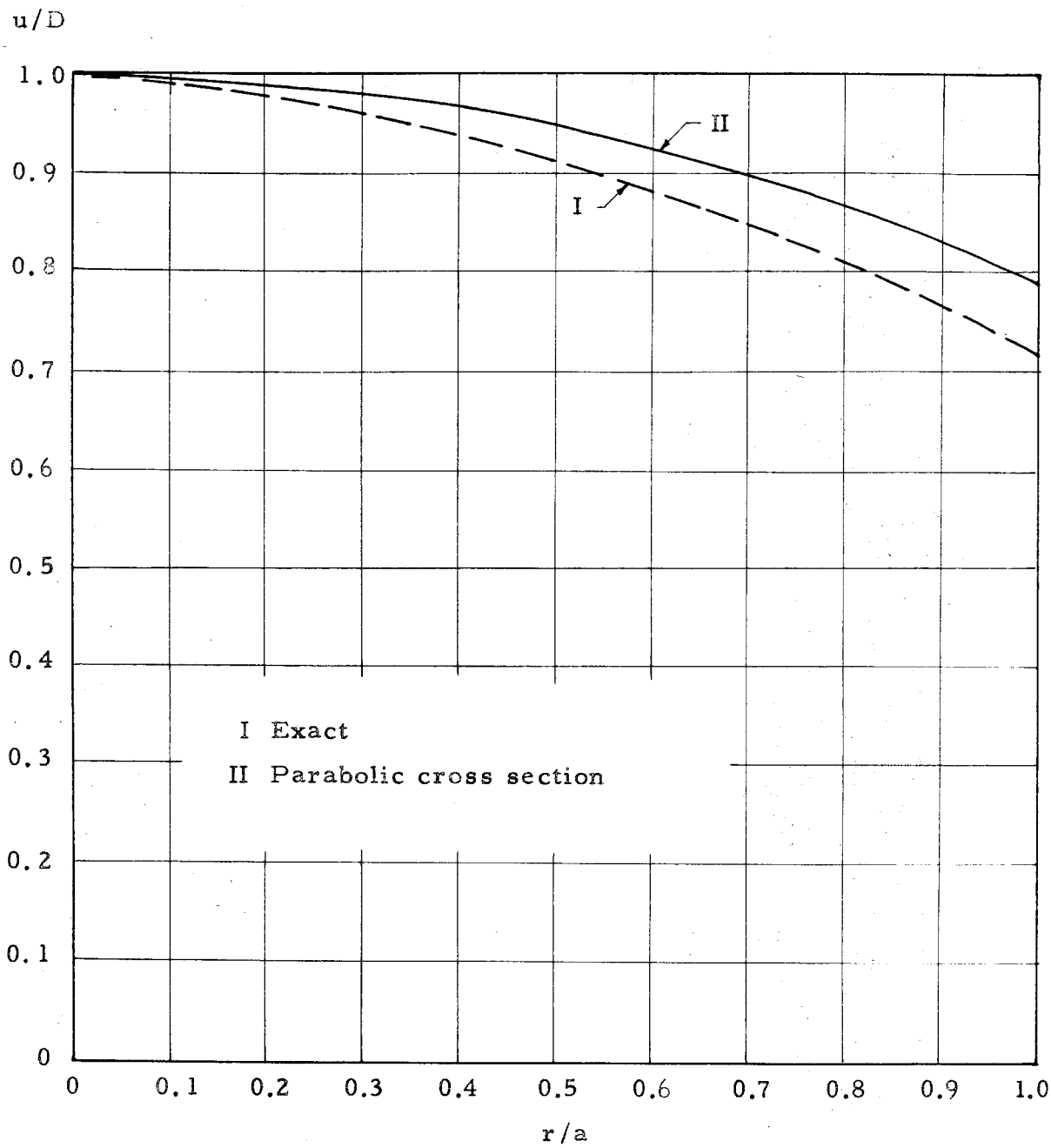

Figure 23. Longitudinal displacement amplitude for $a/\Lambda = 0.196$

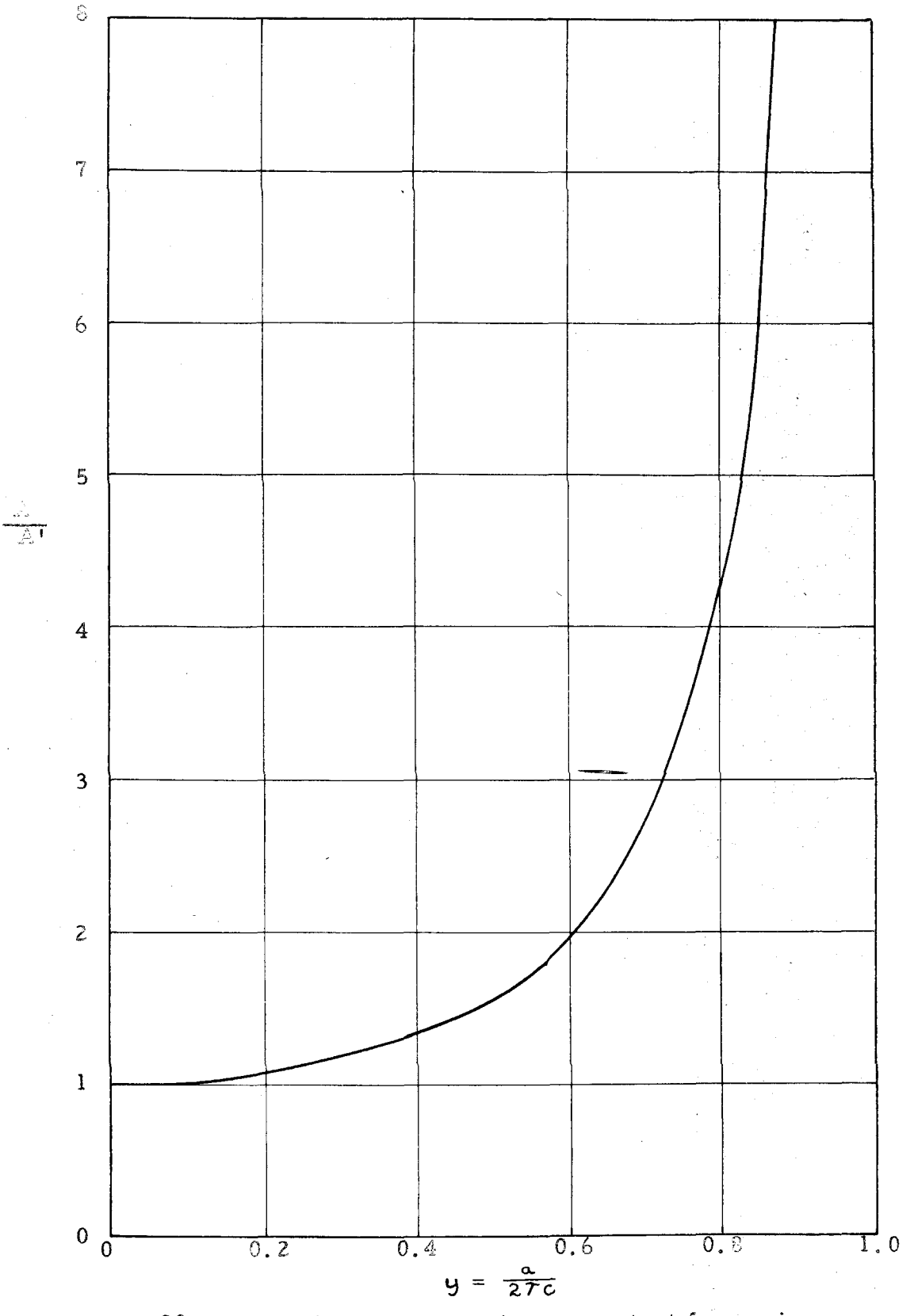

Figure 29. Ratio of strain to strain gage output for various wave length sinusoidal waves.

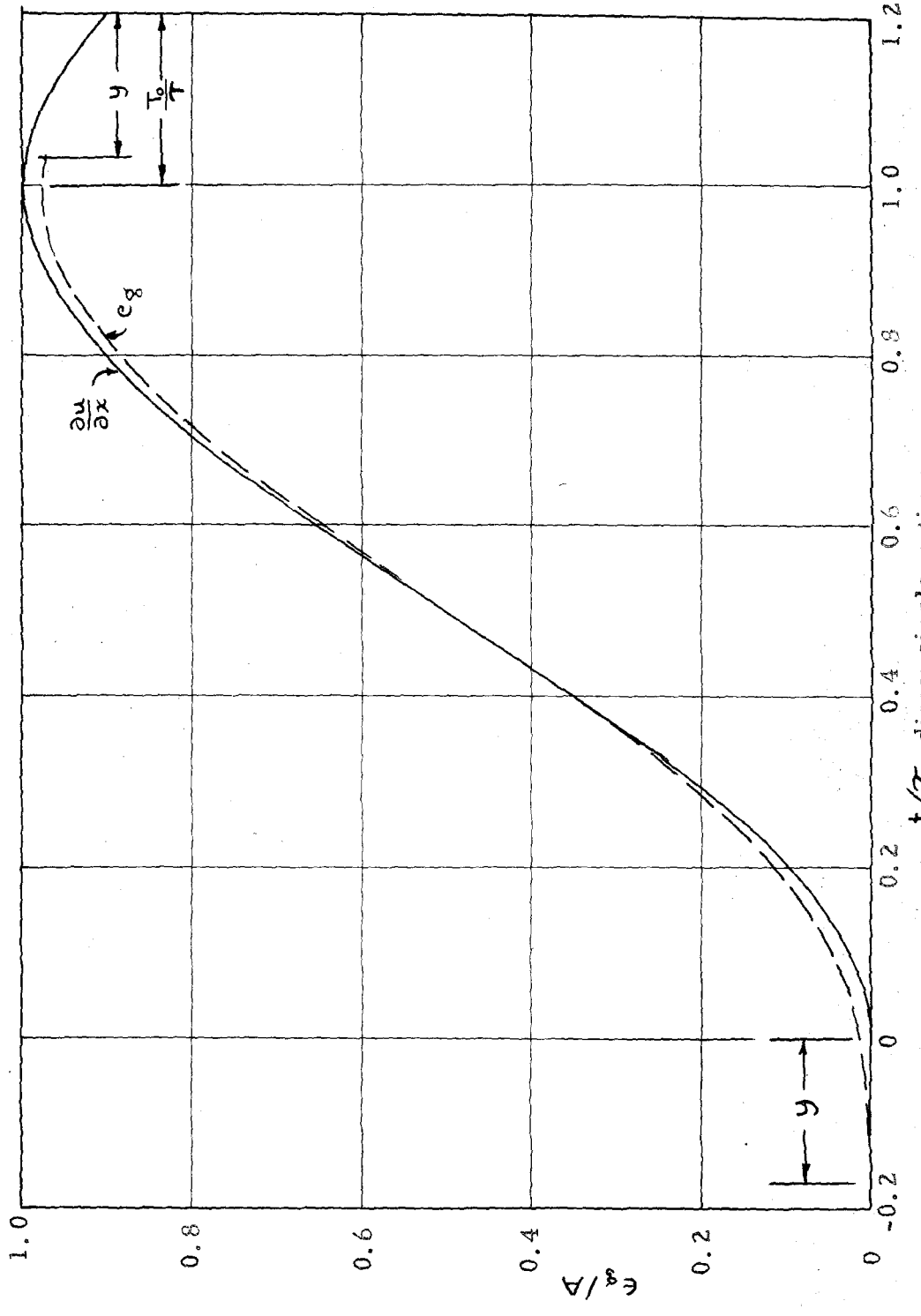

Figure 30 Assumed strain of leading edge of wave vs theoretical indicated strain, for y = 1/6.

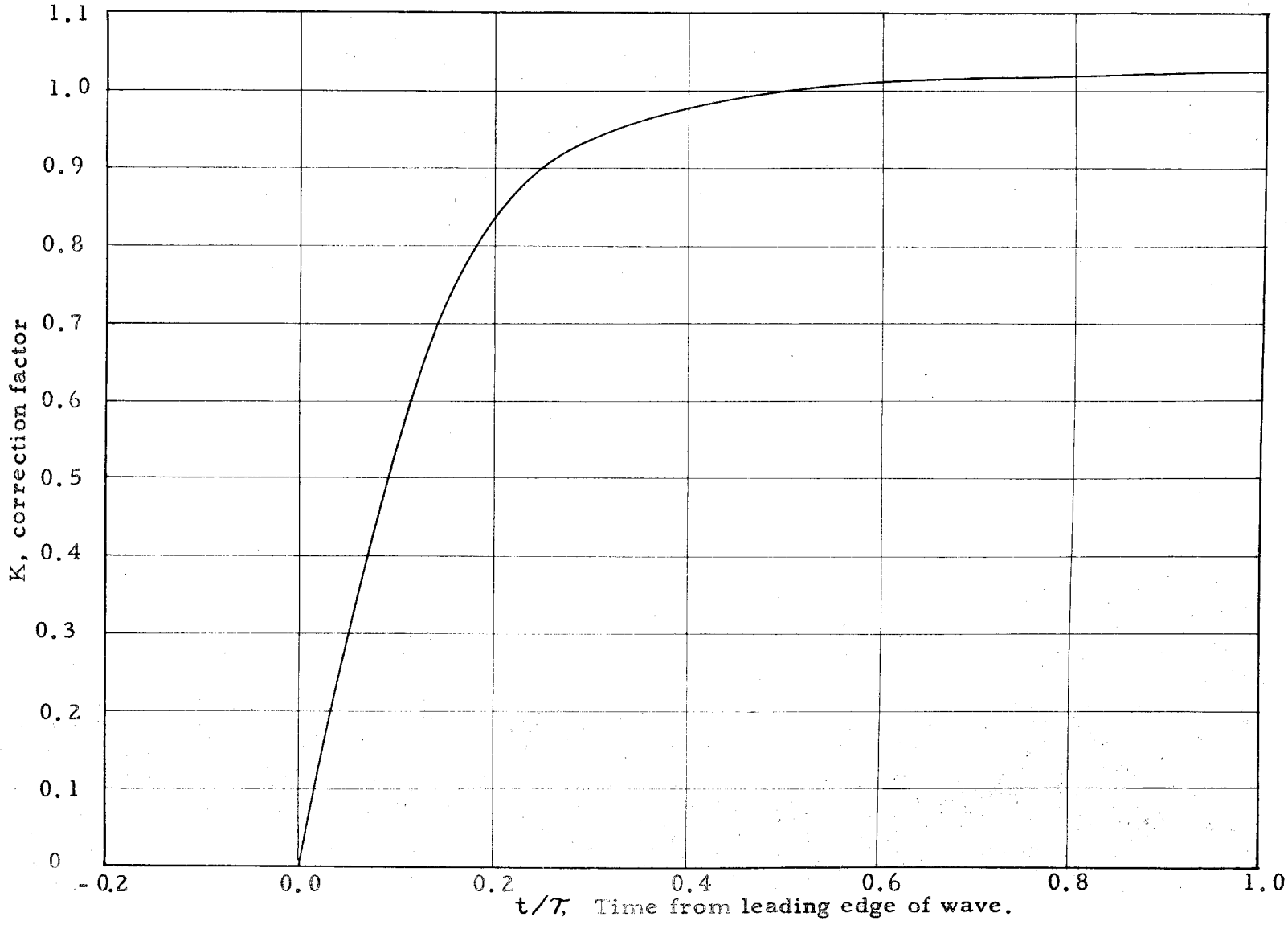

Figure 31. Correction factors K for strain gage signal for leading edge of wave. $\tau \doteq 25$ sec

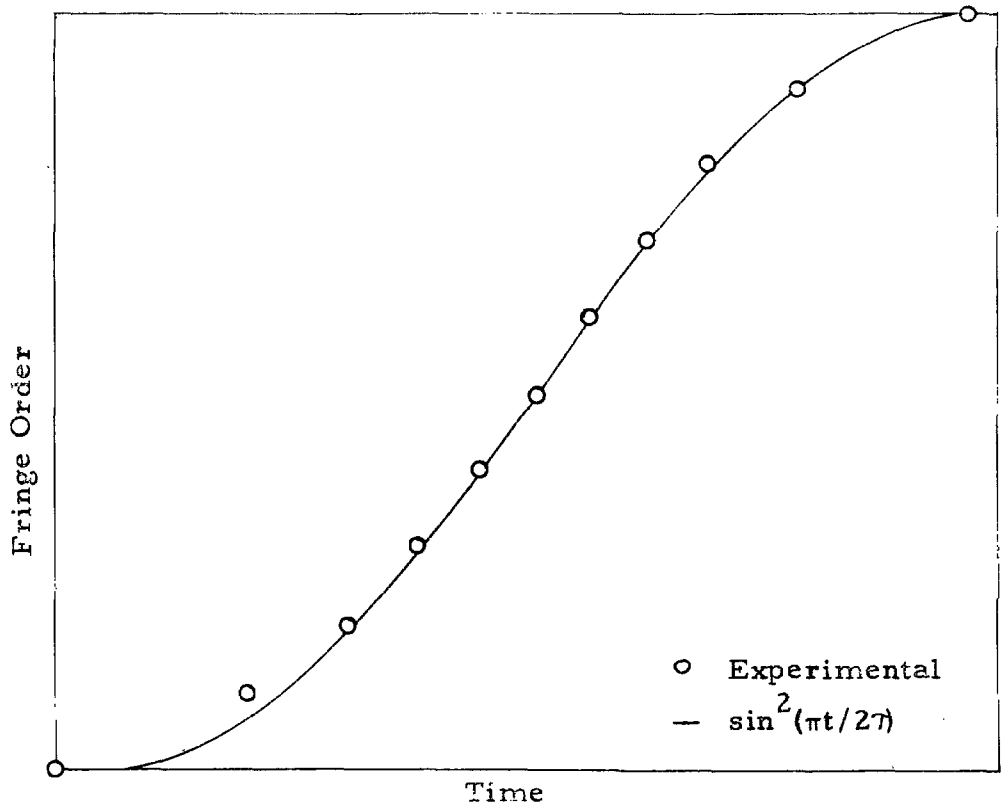

Figure 32. Fringe order of leading edge of stress wave, in comparison to trigonometric form.

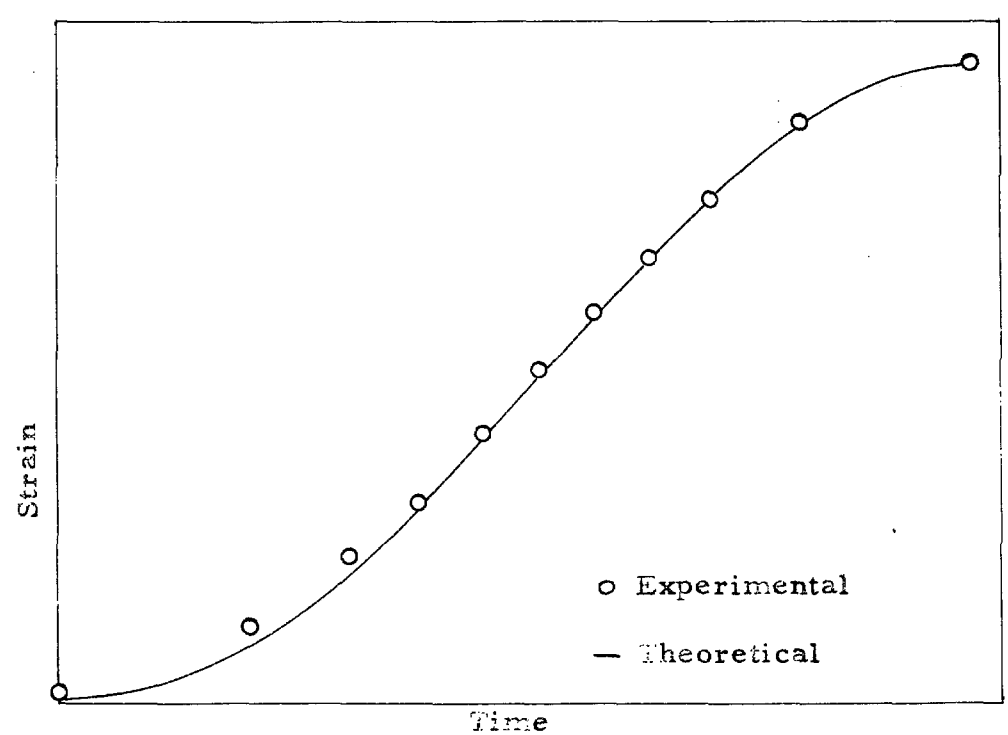

Figure 33. Theoretical strain gage signal vs. experimental strain gage signal.